Mon. Not. R. Astron. Soc. **359,** 1096–1116 (2005) doi:10.1111/j.1365-2966.2005.08973.x

# A survey for planetary transits in the field of NGC 7789

D. M. Bramich,[1,2★] Keith Horne,[1] I. A. Bond,[3,4] R. A. Street,[5] A. Collier Cameron,[1] B. Hood,[1] J. Cooke,[6] D. James,[7,8] T. A. Lister,[1] D. Mitchell,[6] K. Pearson,[9] A. Penny,[10] A. Quirrenbach,[11] N. Safizadeh[6] and Y. Tsapras[12]

[1]*School of Physics and Astronomy, University of St. Andrews, North Haugh, St. Andrews, Fife KY16 9SS*
[2]*Instituto de Astrofisica de Canarias, C/Via Lactea s/n, E-38200 La Laguna,Tenerife, Spain*
[3]*Institute for Astronomy, University of Edinburgh, Royal Observatory, Blackford Hill, Edinburgh EH9 3HJ*
[4]*Institute for Information and Mathematical Sciences, Massey University, Auckland, New Zealand*
[5]*APS Division, Department of Pure and Applied Physics, Queen's University, University Road, Belfast BT7 8NQ*
[6]*Center for Astrophysics and Space Sciences (CASS), University of California, San Diego, 9500 Gilman Drive, La Jolla, CA 92093-0424, USA*
[7]*Laboratoire d'Astrophysique, Observatoire de Grenoble, BP53, F-38041 Grenoble, Cedex 9, France*
[8]*Department of Physics and Astronomy, Vanderbilt University, 1807 Station B, Nashville, TN 37235, USA*
[9]*Louisiana State University, Department of Physics and Astronomy, 202 Nicholson Hall, Tower Drive, Baton Rouge, LA 70803-4001, USA*
[10]*Rutherford Appleton Laboratory, Chilton, Didcot, Oxon OX11 0QX*
[11]*Leiden Observatory, PO Box 9513, NL-2300 RA Leiden, the Netherlands*
[12]*School of Mathematical Sciences, Queen Mary University of London, Mile End Road, London E1 4NS*

Accepted 2005 February 25. Received 2005 February 11; in original form 2004 October 17

**ABSTRACT**

We present results from 30 nights of observations of the open cluster NGC 7789 with the Wide Field Camera on the Isaac Newton Telescope, La Palma. From ∼900 epochs, we obtained light curves and Sloan $r' - i'$ colours for ∼33 000 stars, with ∼2400 stars having better than 1 per cent precision. We expected to detect ∼2 transiting hot Jupiter planets if 1 per cent of stars host such a companion and a typical hot Jupiter radius is ∼1.2 $R_J$. We find 24 transit candidates, 14 of which we can assign a period. We rule out the transiting planet model for 21 of these candidates using various robust arguments. For two candidates, we are unable to decide on their nature, although it seems most likely that they are eclipsing binaries as well. We have one candidate exhibiting a single eclipse, for which we derive a radius of $1.81^{+0.09}_{-0.00}\,R_J$. Three candidates remain that require follow-up observations in order to determine their nature.

**Key words:** methods: data analysis – binaries: eclipsing – Hertzsprung–Russell (HR) diagram – planetary systems – open clusters and associations: general – open clusters and associations: individual: NGC 7789.

## 1 INTRODUCTION

The surprising existence of short-period (∼4 d) Jupiter-mass extrasolar planets (termed 'hot Jupiters'), confirmed by radial velocity measurements in the last decade, has shown us that planetary systems exist in patterns unlike that of our own Solar system. The class of hot Jupiter planets ($P \lesssim 10$ d and $M \sin i \lesssim 10\,M_J$) makes up ∼19 per cent (27 out of 140 as of 2005 February 1) of the planets discovered to date (Schneider 1996), and ∼1 per cent of nearby Solar-type stars host such a companion (Butler et al. 2000). Recently we are starting to see the fruits of current transit surveys. OGLE have produced over 100 transit candidates during two seasons (Udalski et al. 2002a,b, 2003), by far the most prolific transit survey. EXPLORE/OC have produced a handful of transit candidates that are currently being followed up spectroscopically (Mallén-Ornelas et al. 2003), and a search of the MACHO photometry data base has revealed nine transit candidates (Drake & Cook 2004). To date, there are seven confirmed transiting extrasolar planets: HD 209458b (Charbonneau et al. 2000; Brown et al. 2001), discovered first by the radial velocity method; and OGLE-TR-56b (Konacki et al. 2003), OGLE-TR-113b (Bouchy et al. 2004; Konacki et al. 2004), OGLE-TR-132b (Bouchy et al. 2004), OGLE-TR-111b (Pont et al. 2004), TrES-1 (Alonso et al. 2004) and OGLE-TR-10b (Konacki et al. 2005), discovered first by the transit method. The spectroscopic follow-up of the OGLE transit candidates has revealed a new class of short-period planets called the 'very hot Jupiters'. Such planets have periods less than the 3 d cut-off identified in the sample of radial velocity planets.

In order to discover transiting hot Jupiters through a photometric survey, one requires high-cadence, high-accuracy observations ($\lesssim$1 per cent accuracy per data point with a duty cycle $\gtrsim$8 data points per hour) of many stars ($>10^4$) simultaneously over long observing runs (>10 nights). Any transit candidates (stars

★E-mail: dmb7@st-and.ac.uk

that show at least one eclipse event) may be subsequently followed up by radial velocity (RV) measurements in order to determine the companion mass, or at least an upper limit to the mass. However, owing to the long integration times on large telescopes required for RV follow-up and the high frequency of planetary transit mimics, it is prudent to try to rule out the transiting planet model for as many transit candidates as possible via simple supplementary observations and/or further analysis of the light curve (Sirko & Paczyński 2003; Drake 2003; Charbonneau 2003; Charbonneau et al. 2004).

The study of open clusters for transiting planets has a number of advantages over fields in other parts of the sky or Galactic plane. While providing a relatively large concentration of stars on the sky (but not so large as to cause blending problems as in the case of globular clusters observed from the ground), they also provide a set of common stellar parameters for the cluster members. These are metallicity, age, stellar crowding and radiation density. Also, the fainter cluster members are smaller stars and therefore they are likely to show deeper transit signatures, helping to offset sky noise contributions. The identification of the cluster main sequence in the colour–magnitude diagram allows the assignment of a model-dependent mass and radius to each photometric cluster member, and, assuming a law relating extinction to distance for the field, allows the assignment of a model-dependent mass, radius and distance to all stars in the field under the assumption that they are main-sequence stars. Transit candidates with well-defined phased light curves may therefore be analysed in detail as to whether they are consistent with a transiting planet model. An estimate of the fraction of stars hosting a hot Jupiter (referred to as the 'hot Jupiter fraction') may be obtained by comparing the number of hot Jupiters that are actually detected to how many one would expect to detect using the knowledge of the star properties and the light curves themselves. The dependence of the hot Jupiter fraction on the cluster parameters may then be investigated by extending the experiment to other open clusters.

Currently, there are a number of groups searching for transiting planets in open clusters (von Braun et al. 2004a). These include UStAPS (Street et al. 2003; Hood et al. 2005; this paper), EXPLORE/OC (Mallén-Ornelas et al. 2003; Lee et al. 2004; von Braun et al. 2004b), STEPSS (Burke et al. 2004) and PISCES (Mochejska et al. 2002, 2004). A number of transit candidates have been put forward by these groups, but none have been confirmed as transiting planets so far. In this survey, as with open cluster transit surveys in general, we are photometrically observing faint stars (16 to 21 mag). This makes follow-up observations difficult but not impossible. However, many of the stars observed are of later spectral types than those probed by the RV surveys, since RV surveys are limited to bright solar-neighbourhood FGK stars. In particular, our survey of NGC 7789 probes the spectral types F5 to M5 (see Fig. 2), including a large proportion of K and M stars. Furthermore, we are searching for planets out to distances well beyond the solar neighbourhood.

The observations of open cluster NGC 7789 is the subject of this paper. The main parameters of the cluster are shown in Table 1. For a good review of previous relevant work on this cluster, see Gim et al. (1998). In Section 2 we report on the observations made, in Section 3 we present in detail the data reduction/photometry, in Section 4 we present the astrometry and colour data, in Section 5 we describe the transit detection algorithm, and in Section 6 we present a detailed analysis of the transit candidates. Finally, in Section 7 we outline our conclusions and future work.

**Table 1.** Properties of the open cluster NGC 7789. Data taken from http://obswww.unige.ch/webda by J. C. Mermilliod and the Simbad data base.

| | |
|---|---|
| RA (J2000.0) | $23^{\rm h}57^{\rm m}$ |
| Dec. (J2000.0) | $+56^\circ43'$ |
| $l$ | $115\overset{\circ}{.}48$ |
| $b$ | $-5\overset{\circ}{.}37$ |
| Distance | 2337 pc |
| Radius | ∼16 arcmin |
| Age | 1.7 Gyr |
| [Fe/H] | −0.08 |
| $E(B-V)$ | 0.217 |

## 2 OBSERVATIONS

We observed the open cluster NGC 7789 (see Table 1) using the 2.5-m Isaac Newton Telescope (INT) of the Observatorio del Roque de los Muchachos, La Palma, Canary Islands, during three bright runs with dates 1999 June 22–30, 1999 July 22–31 and 2000 September 10–20. For brevity, these runs will be referred to from now on as 1999–06, 1999–07 and 2000–09, respectively. We used the Wide Field Camera (WFC), which consists of a four charge-coupled device (CCD) mosaic, where each CCD is 2048 × 4096 pixels (Walton et al. 2001). The pixel scale is 0.33 arcsec pixel$^{-1}$ and the field of view is ∼0.5 × 0.5 deg$^2$. The gain and readout noise values for each chip were calculated automatically during the preprocessing stage of the data reduction (see Section 3.1). The mosaic field was centred on NGC 7789 at RA $\alpha = 23^{\rm h}57^{\rm m}30^{\rm s}$ and Dec. $\delta = +56^\circ43'41''$.

The usual procedure for each night was to obtain ∼5 bias frames and ∼8 sky flat frames at both the beginning and end of the night. Observations on NGC 7789 in the runs 1999–06 and 1999–07 consisted of ∼6 pairs of 300-s exposures taken every ∼50 min during the later part of each night. Observations in the 2000–09 run consisted of sequences of 10 consecutive 300-s exposures followed by a bias frame, repeated continuously throughout the whole of each night. With a readout time of 100 s and various losses due to bad weather/seeing and telescope jumps, this resulted in a total of 880 300-s exposures in Sloan $r'$ over the three runs, with 691 of these exposures from the 2000–09 run alone. During the 2000–09 run, we also took five images of NGC 7789 with varying exposure times in Sloan $i'$, along with five sky flat frames, in order to provide us with the necessary colour information.

## 3 CCD REDUCTIONS

### 3.1 Preprocessing: CCD calibrations

Each run and each chip was treated independently for the purpose of the reductions. The reduction process was carried out by a single C-shell/IRAF script that runs according to a user-defined parameter file. Bad pixels were flagged in a user-defined detector bad pixel mask, and ignored where relevant. The reductions consisted of the standard bias subtraction and flat fielding of the science frames using appropriate master calibration frames. The gain and readout noise of each chip were also determined during the reductions.

### 3.2 Photometry: difference image analysis

Differential photometry on the reduced science frames in the Sloan $r'$ filter was accomplished using the method of difference image analysis (Alard & Lupton 1998; Alard 2000). Our implementation of this procedure was adapted from the code written for the MOA

project (Bond et al. 2001), and it consists of three automated scripts. The process is described below in relative detail since the same procedure has subsequently been used on many other data sets (e.g. Arellano Ferro et al. 2004). Bad pixels are ignored in the operations that the scripts perform.

(i) The first script constructs a reference frame from selected frames with good seeing, and a star list from the reference frame. First, stars are detected and matched between the best seeing frames in order to derive a set of linear transformations and geometrically align the frames. The frames are then combined into a mean reference frame using the exposure times of the individual images as weights. The reference frame is analysed using IRAF's package DAOPHOT (Stetson 1987). The package identifies stars on the reference frame and chooses a set of 175 point spread function (PSF) stars. A 'penny2' PSF function that varies quadratically with position, along with a lookup table of residuals, is solved for. The neighbours of the PSF stars are then subtracted using this solution, and a new PSF function is solved for. This new solution is used to measure the instrumental fluxes and positions of all stars on the reference frame. The result is a reference frame with a corresponding star list. We used 13 consecutive best seeing images ($\sim$1 arcsec) to construct the reference frame.

(ii) The reference frame is used to produce a set of difference images. The main idea behind difference image analysis is that an image frame $I(x, y)$ is related to the reference frame $R(x, y)$ via the following equation:

$$I(x, y) = R \otimes K(x, y) + B(x, y), \tag{1}$$

where

$$R \otimes K(x, y) \equiv \iint R(x-u, y-v)\, K(u, v, x, y)\, \mathrm{d}u\, \mathrm{d}v. \tag{2}$$

Here $B(x, y)$ represents the change in the sky background and $K(u, v, x, y)$ is a spatially varying convolution kernel relating the PSF on the reference frame to the PSF on the image frame at spatial position $x, y$. We model the convolution kernel

$$K(u, v, x, y) = \sum_i a_i(x, y)\, b_i(u, v) \tag{3}$$

as the sum of a set of basis functions $b_i(u, v)$ each formed as a product of a two-dimensional Gaussian function of $u$ and $v$ with a polynomial of degree 2 in $u$ and $v$. For the basis functions we use three Gaussian components with $\sigma$ values of 2.1, 1.3 and 0.7 pixels and associated polynomial degrees of 2, 4 and 6, respectively. To allow for the kernel's spatial dependence, the coefficients $a_i(x, y)$ are polynomials of degree 2 in $x$ and $y$. The kernel is also normalized to a constant integral over $u$ and $v$ for each $x$ and $y$, thus ensuring a constant photometric scalefactor between the reference frame and image frame. We model the differential sky background $B(x, y)$ as a polynomial of degree 2 in $x$ and $y$. We solve for $K(u, v, x, y)$ and $B(x, y)$ in the least-squares sense for each science frame by fitting to pixel boxes around selected bright stars distributed uniformly across the reference frame. The kernel is assumed to be independent of $x$ and $y$ within each box. A difference image is then constructed for each science frame by rearranging equation (1) to the following form and using the solutions for $K(u, v, x, y)$ and $B(x, y)$:

$$D(x, y) = I(x, y) - R \otimes K(x, y) - B(x, y). \tag{4}$$

The difference image $D(x, y)$ should simply be an image representative of the Poisson noise in $I(x, y)$. However, any objects that have varied in brightness in comparison to the reference frame should show up as positive or negative pixel areas on the difference image, which may be measured to obtain the differential flux. In our analysis, each chip was split up into eight square sections and the difference image constructed from solving for the kernel and differential sky background in each section. Also, a high signal-to-noise ratio empirical PSF for the reference frame is constructed in each section by stacking up a set of stamps centred on suitable bright stars.

(iii) The third script measures the differential flux on each difference image via optimal PSF scaling at the position of each star. The normalized and sky-subtracted empirical PSF constructed for each square section of the reference frame in step (ii) is convolved with the kernel corresponding to the current difference image section. The convolved PSF is optimally scaled, at the position of the current star, to the difference image. A $3\sigma$ clip on the residuals of the scaling is performed, and one pixel rejected. The scaling and rejection is repeated until no more pixels are rejected. The differential flux is measured as the integral of this scaled PSF.

A light curve for each star was constructed by the addition of the differential fluxes to the star fluxes as measured on the reference frame. The following equations were used:

$$f_{\mathrm{tot}}(t) = f_{\mathrm{ref}} + \frac{f_{\mathrm{diff}}(t)}{p(t)}, \tag{5}$$

$$m(t) = 25.0 - 2.5 \log[f_{\mathrm{tot}}(t)], \tag{6}$$

where $f_{\mathrm{tot}}(t)$ is the star flux (ADU $\mathrm{s}^{-1}$) at time $t$, $f_{\mathrm{ref}}$ is the star flux (ADU $\mathrm{s}^{-1}$) as measured on the reference frame, $f_{\mathrm{diff}}(t)$ is the differential flux (ADU $\mathrm{s}^{-1}$) at time $t$ as measured on the difference image, $p(t)$ is the photometric scalefactor (the integral of the kernel solution over $u$ and $v$) at time $t$, and $m(t)$ is the magnitude of the star at time $t$. Uncertainties are propagated in the correct analytical fashion.

Flux measurements were rejected for a $\chi^2\,\mathrm{pixel}^{-1} \geqslant 5.0$ for the PSF scaling, and for PSFs with a full width at half-maximum FWHM $\geqslant 7.0$ pixels, in order to remove bad measurements. Hence, all the stars have differing numbers of photometric measurements. In each run, light curves with less than half of the total possible epochs were rejected. For the 2000–09 run this analysis produced 8631 light curves on chip 1, 7625 light curves on chip 2, 8411 light curves on chip 3, and 8830 light curves on chip 4 (centred on the cluster). Fig. 1 shows a diagram of the rms scatter in the light curves against instrumental magnitude for the 2000–09 run for each chip. Similar diagrams were produced for the 1999–06 and 1999–07 runs but are not shown here for brevity.

Since each run was treated independently for the reductions, each chip has three different reference frames, and hence each star has three different reference magnitudes. For a particular star, let us denote the reference magnitude from the 2000–09 run minus the reference magnitude from the 1999–06 run by $\Delta m_1$, and the reference magnitude from the 2000–09 run minus the reference magnitude from the 1999–07 run by $\Delta m_2$. For each chip, we have calculated the unweighted mean of $\Delta m_1$ and $\Delta m_2$ over all stars on that chip. We then added the resulting $\overline{\Delta m_1}$ and $\overline{\Delta m_2}$ to the light-curve data points in the 1999–06 and 1999–07 runs, respectively. The values of the means, $\overline{\Delta m_1}$ and $\overline{\Delta m_2}$, for each chip along with the standard deviations about the means, $\sigma_1$ and $\sigma_2$, respectively, are presented in Table 2.

As can be seen from Fig. 1, we have obtained high-precision photometry with an rms accuracy of $\sim$3–5 mmag at the bright end. Most stars are limited by sky noise because all three runs were during bright time. However, the 'backbone' of points on each diagram lies

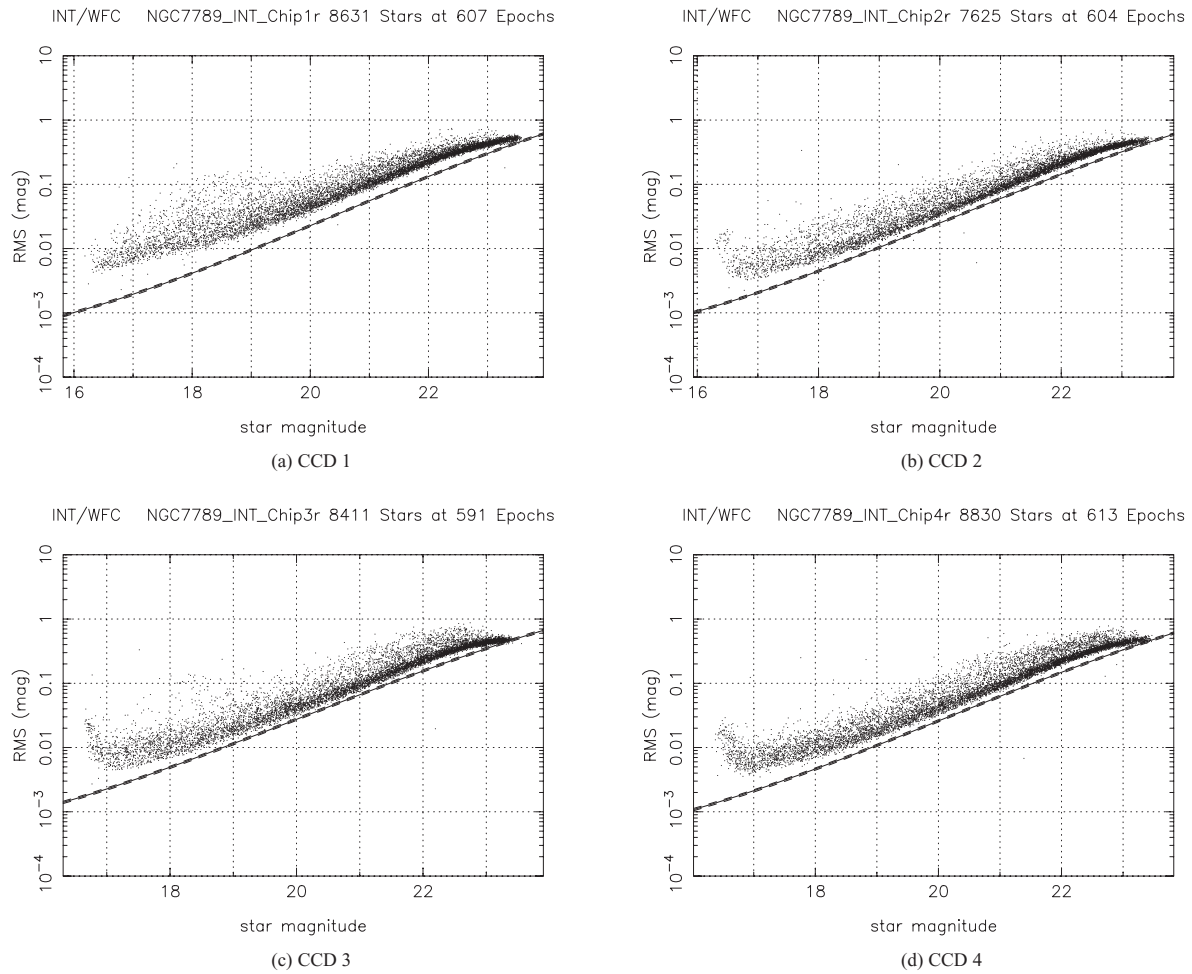


(a) CCD 1 (b) CCD 2

(c) CCD 3 (d) CCD 4

**Figure 1.** Plots of standard deviation (rms) of the light curves against mean instrumental Sloan $r'$ magnitude for all stars from each chip for the 2000–09 run. The lower curve in each diagram represents the theoretical noise limit for photon and readout noise.

**Table 2.** Magnitude offsets $\overline{\Delta m_1}$ and $\overline{\Delta m_2}$ added to the light-curve data points from the 1999–06 and 1999–07 runs, respectively.

| Chip No. | $\overline{\Delta m_1}$ | $\sigma_1$ | $\overline{\Delta m_2}$ | $\sigma_2$ |
|---|---|---|---|---|
| 1 | −0.832 | 0.037 | −0.753 | 0.041 |
| 2 | −0.698 | 0.036 | −0.843 | 0.043 |
| 3 | −0.596 | 0.031 | −0.404 | 0.054 |
| 4 | −0.527 | 0.036 | −0.470 | 0.037 |
| Run | 1999–06 | | 1999–07 | |

above the theoretical limit by a factor of ∼1.5–2.0 depending on the chip being considered. We put this down to systematic errors in the data due to a subset of low-quality difference images and/or sections of difference images that were produced from science frames taken on nights of poor quality seeing/atmospheric conditions.

## 4 ASTROMETRY AND COLOUR DATA

### 4.1 Astrometry

Astrometry was undertaken by matching 358 stars from the four reference frames (one for each chip) with the USNO-B1.0 star catalogue (Monet et al. 2003) using a field overlay in the image display tool GAIA (Draper 2000). The WFC suffers from pin-cushion distortion; hence it was necessary to fit a nine-parameter astrometric solution to the reference frames in order to obtain sufficiently accurate celestial coordinates for all the stars. The nine parameters are made up of six parameters to define the linear transformation between pixel coordinates and celestial coordinates, two parameters to define the plate centre and one parameter to define the radial distortion coefficient. The Starlink package ASTROM (Wallace 1998) was used to perform the fit, and the achieved accuracy was ∼0.4 arcsec rms radially for the 358 matching stars. The astrometric fit was then used to calculate the J2000.0 celestial coordinates for all stars with a light curve.

### 4.2 Colour indices

The best image in the Sloan $i'$ filter was aligned with the Sloan $r'$ reference frame for each chip and the magnitudes of the stars were measured using DAOPHOT PSF fitting in the same way as they were measured on the reference frame in Section 3.2. Table 3 shows the number of stars with light curves that have Sloan $r' - i'$ colour indices as a result.

### 4.3 Colour–magnitude diagrams

Figs 2(a)–(d) show an instrumental colour–magnitude diagram (CMD) for each chip. The cluster main sequence is clearly visible.

**Table 3.** Number of stars with a Sloan $r'$ light curve, and the number of such stars with a Sloan $r' - i'$ colour index.

| Chip No. | No. stars with a light curve | No. stars with a light curve and an $r' - i'$ colour index | Percentage |
|---|---|---|---|
| 1 | 8631 | 8497 | 98.4 |
| 2 | 7625 | 7576 | 99.4 |
| 3 | 8411 | 8290 | 98.6 |
| 4 | 8830 | 8672 | 98.2 |
| Total | 33497 | 33035 | 98.6 |

Chip 4 is centred on the cluster and as expected shows the strongest cluster main sequence. A theoretical cluster main sequence is plotted on each diagram over the cluster main sequence. We have used the theoretical models of Baraffe et al. (1998) for the stellar mass range $0.60\,\mathrm{M}_\odot \leqslant M_* \leqslant 1.40\,\mathrm{M}_\odot$, the age of the cluster (1.7 Gyr) and solar-type metallicity [M/H] = 0 in order to predict the main-sequence absolute magnitudes, colours and radii. Below a mass of $0.60\,\mathrm{M}_\odot$, the Baraffe model predicts $R - I$ colours substantially bluer than the observed cluster main sequence, a limitation noted in Baraffe et al. (1998). As a result, we used data from Lang (1992) for the stellar mass range $0.08\,\mathrm{M}_\odot \leqslant M_* \leqslant 0.60\,\mathrm{M}_\odot$. The combined model for the cluster main sequence supplies an absolute magnitude $M_R$, an absolute magnitude $M_I$ and a stellar radius $R_*$ for the stellar mass range $0.08\,\mathrm{M}_\odot \leqslant M_* \leqslant 1.40\,\mathrm{M}_\odot$. We interpolated this combined model with cubic splines.

The interstellar medium (ISM) in the Milky Way is mostly concentrated in the Galactic plane, and the density law governing its mean distribution (ignoring small-scale variations) can be modelled by an Einasto law:

$$\rho(R, z) = \rho_0 \exp\left[-\left(\frac{R - \mathrm{R}_\odot}{h_R}\right)\right] \exp\left(-\frac{|z|}{h_z}\right), \tag{7}$$

where $R$ is the Galactocentric distance, $z$ is the height above the Galactic plane, $\rho_0$ is the local density of the ISM, $\mathrm{R}_\odot$ is the distance of the Sun from the Galactic Centre, $h_R$ is the ISM density scaleheight in the $R$ direction, and $h_z$ is the ISM density scaleheight in the $z$ direction. One may derive the density $\rho$ of the ISM as a function of distance $d$ from the Sun in the direction of the open cluster NGC 7789 by using trigonometric arguments to rewrite $R$ and $z$ as functions of $d$. In this derivation, we have assumed that the Sun has Galactic coordinates $(R, z) = (8.5\,\mathrm{kpc}, 0.015\,\mathrm{kpc})$ and that $\rho_0 = 0.021\,\mathrm{M}_\odot\,\mathrm{pc}^{-3}$, $h_R = 4.5\,\mathrm{kpc}$ and $h_z = 0.14\,\mathrm{kpc}$ as given in Robin et al. (2003). In any wave band, the total extinction $A$ as a function of $d$ is proportional to the integral of $\rho(d)$ over $d$. Hence, absorbing the constant $\rho_0$ into a new constant $K$ we have

$$A(d) = K \int_0^d \rho(u)\,\mathrm{d}u. \tag{8}$$

Adopting $E(B - V) = 0.217$ for the cluster (Table 1), we calculate the corresponding extinction to be $A_R \approx 0.547$ and $A_I \approx 0.429$ in the $R$ and $I$ bands, respectively, evaluated with a synthetic photometry code (XCAL) using a Galactic extinction curve from Seaton (1979). This extinction applies to stars at the cluster distance $d_\mathrm{c} = 2337\,\mathrm{pc}$, and hence, by numerically evaluating the integral in equation (8), we may calculate values for $K$ that apply to the $R$ and $I$ bands as $K_R = 2.20 \times 10^{-2}\,\mathrm{mag\,M}^{-1}{}_\odot\,\mathrm{pc}^2$ and $K_I = 1.73 \times 10^{-2}\,\mathrm{mag\,M}^{-1}{}_\odot\,\mathrm{pc}^2$, respectively.

We have used the law relating extinction to distance as given in equation (8) to correct the absolute magnitudes $M_R$ and $M_I$ of the theoretical main sequence to the observed magnitudes $R(d)$ and $I(d)$, respectively. In the following equations, the distance $d$ has units of parsecs (pc):

$$R(d) = M_R + 5\log(d) - 5 + A_R(d), \tag{9}$$

$$I(d) = M_I + 5\log(d) - 5 + A_I(d), \tag{10}$$

where $A_R(d)$ and $A_I(d)$ are versions of equation (8) with $K = K_R$ and $K = K_I$, respectively.

Conversions between the Johnson–Cousins $R$ and $I$ magnitudes and the Sloan $r'$ and $i'$ magnitudes were done using the following predetermined relations presented on the Cambridge Astronomical Survey Unit (CASU) website:[1]

$$r' = R + 0.275(R - I) + 0.008, \tag{11}$$

$$r' - i' = 1.052(R - I) + 0.004. \tag{12}$$

As a result of the lack of observations of standard stars, it was necessary to fit the interpolated theoretical main sequence to the cluster main sequence on the CMD for each chip by eye, after correcting for the cluster distance and extinction, via simple $r'$ and $r' - i'$ offsets. These offsets are displayed in Table 4. Note that the required horizontal and vertical shifts are correlated, since shifts parallel to the main sequence would have no effect if the main sequence were a straight line. Fortunately, the kink (change of slope) in the main sequence near the spectral type K0 ($0.8\,\mathrm{M}_\odot$) allows us to estimate both vertical and horizontal shifts. This feature is clearly visible on all four chips.

### 4.4 Stellar masses, radii and distances

The identification of the cluster main sequence on each CMD allows a model-dependent mass, radius and distance for each star to be determined using the theoretical main sequence, assuming that each star is a main-sequence star. Giant stars (MK luminosity class III) have absolute magnitudes in the range $1.7 \leqslant M_V \sim M_R \leqslant -6.5$ (Lang 1992). Assuming that the Sun lies in the Galactic plane at a distance of 8.5 kpc from the Galactic Centre (the IAU value), and assuming that the Galactic disc has a radius of 14.0 kpc (Robin, Crézé & Mohan 1992), then the distance to the edge of the Galaxy in the direction of NGC 7789 may be calculated as ∼8.1 kpc using elementary trigonometry. The magnitude of the dimmest giant at 8.1 kpc assuming no extinction is $R = 16.2$ and, assuming the law relating extinction to distance in equation (8), the dimmest giant has a magnitude of $R = 16.9$. These faint limits are marked on the CMDs in Figs 2(a)–(d) as dotted lines. From this simple argument, it can be seen that only the brightest stars in our sample will be contaminated with giant stars.

In principle, for each star on the CMD, it is possible to choose a value for the distance parameter $d$ in equations (9) and (10) such that the theoretical main sequence passes through the star's position on the CMD. The solution $d = d_*$ is then the distance to the star. The star mass $M_*$ and radius $R_*$ may subsequently be determined from where the star lies on the theoretical main sequence at a distance of $d_*$. Fig. 2(e) shows the grid of star masses and distances used for chip 4. The solid 'vertical' lines represent lines of constant stellar mass (and radius), and are labelled at the top of the diagram in units of $\mathrm{M}_\odot$. The 'diagonal' dashed lines represent theoretical main-sequence models at different distances, and the distances are labelled to the right and bottom of the diagram in units of parsecs. Fiducial

[1] http://www.ast.cam.ac.uk/∼wfcsur/index.php

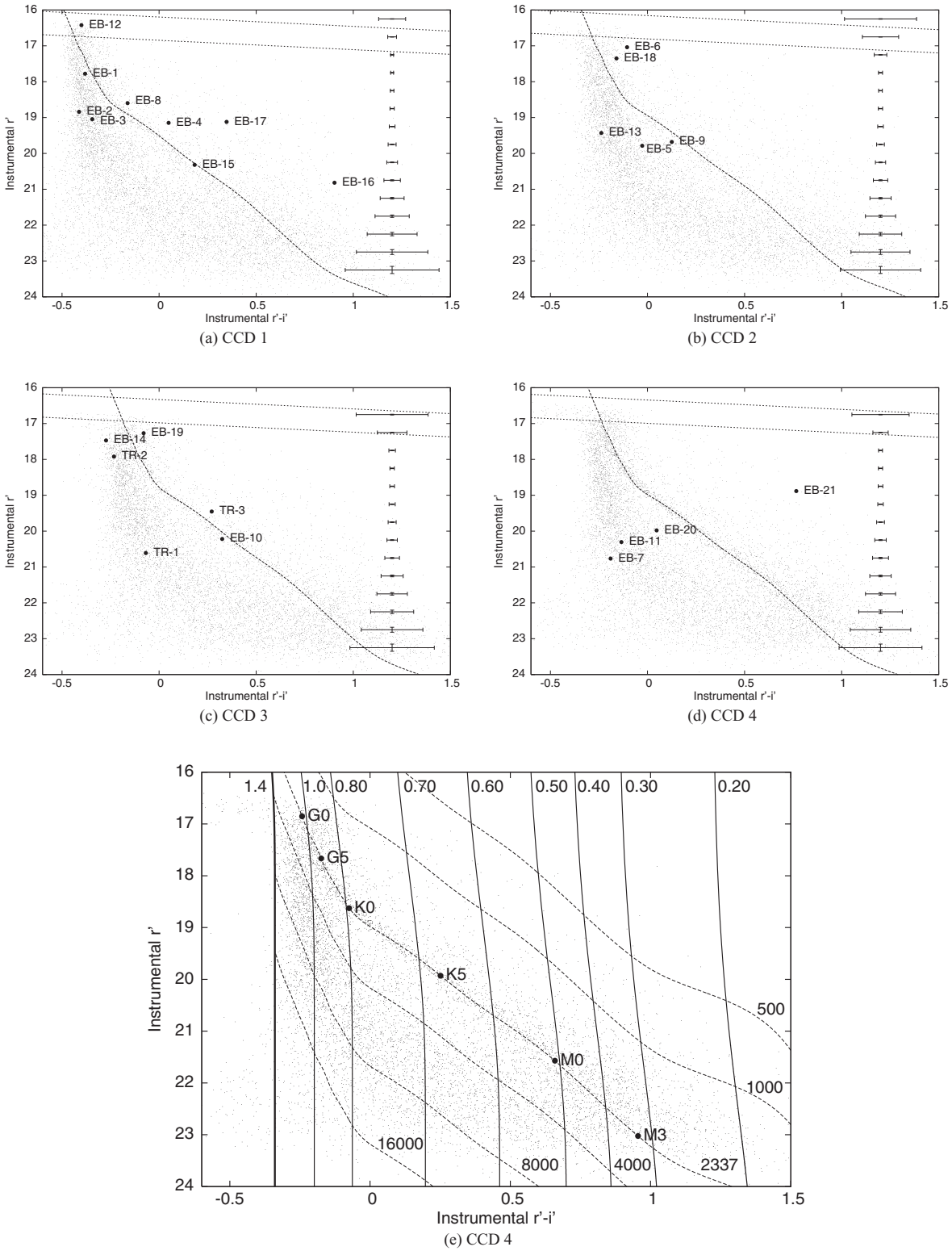


**Figure 2.** (a)–(d) Instrumental CMDs for all stars from each chip for the 2000–09 run. The main sequence is visible on each chip, and the theoretical cluster main sequence is overlaid as the dashed line. The straight dotted lines are the faint limits for giant stars assuming no extinction and the law relating extinction to distance in equation (8). The transit candidates of Section 6 are marked as solid circles. The error bars on the right-hand side of each diagram represent the mean error bar on each measurement for 0.5 mag bins. (e) Instrumental CMD for chip 4 (see Section 4.4). The numbers along the top are masses in units of $M_{\odot}$ and the numbers along the bottom and right are distances in parsecs.

**Table 4.** Offsets determined by eye between observed $r'_{\rm obs}$ and $r'_{\rm obs} - i'_{\rm obs}$ magnitudes, and theoretical $r'(d_{\rm c})$ and $r'(d_{\rm c}) - i'(d_{\rm c})$ main-sequence magnitudes for the cluster distance $d_{\rm c}$.

| Chip No. | $r'_{\rm obs} - r'(d_{\rm c})$ | $[r'_{\rm obs} - i'_{\rm obs}] - [r'(d_{\rm c}) - i'(d_{\rm c})]$ |
|---|---|---|
| 1 | −0.3 | −0.95 |
| 2 | −0.3 | −0.80 |
| 3 | −0.1 | −0.70 |
| 4 | −0.1 | −0.75 |
| Estimated error | ±0.1 | ±0.05 |

spectral types are marked on the cluster theoretical main sequence for clarity.

Because of the steepness of the theoretical main sequence in the CMD for star masses greater than $0.80\,{\rm M}_{\odot}$, the determined star properties become more uncertain above $0.80\,{\rm M}_{\odot}$. Also, the theoretical main sequence that we have used terminates at a mass of $1.40\,{\rm M}_{\odot}$, which leads to a small region where there are no solutions for $d_*$. In Fig. 2(e), this region is blueward of the thick continuous line (corresponding to a mass of $1.40\,{\rm M}_{\odot}$). Stars with no solution for $d_*$ have masses greater than $1.40\,{\rm M}_{\odot}$ (and radii greater than $1.70\,{\rm R}_{\odot}$) and large distances. It is around these stars that it is hardest to detect a transiting planet, and hence a lack of solution for $d_*$, $M_*$ and $R_*$ will hardly affect the completeness of our survey. Table 6 shows the star masses, radii and distances obtained by the above procedure for the transit candidates discussed in Section 6. The star $r' - i'$ colours have been corrected where necessary for any light-curve variations (since the reference frame from which the $r'$ magnitude was determined has a different epoch to the $i'$ frame from which the $i'$ magnitude was determined).

In Figs 3(a) and (b) we plot the $r'$ magnitude and standard deviation (rms) of the light curve of each star versus the stellar radius derived from the main-sequence model and the observed $r' - i'$ colour index. A vertical stripe of stars is evident with $R_* \sim 0.75\,{\rm R}_{\odot}$. This arises because of a relatively rapid change in the colour index with mass for the theoretical main sequence in this mass range. This effect is also evident in Fig. 2(e), where the vertical isomass lines are more widely spaced for $0.5\,{\rm M}_{\odot} < M_* < 0.8\,{\rm M}_{\odot}$. If the mass function and mass–radius relationship for main-sequence stars are both smooth, then this effect represents a deficiency in the $R - I$ colour index of the stellar models.

### 4.5 The expected number of transiting planets

In Fig. 3(b) each point below one of the curves represents a star whose light curve has sufficient accuracy in our data set to reveal transits by HD 209458b-like planets of the indicated radius. To

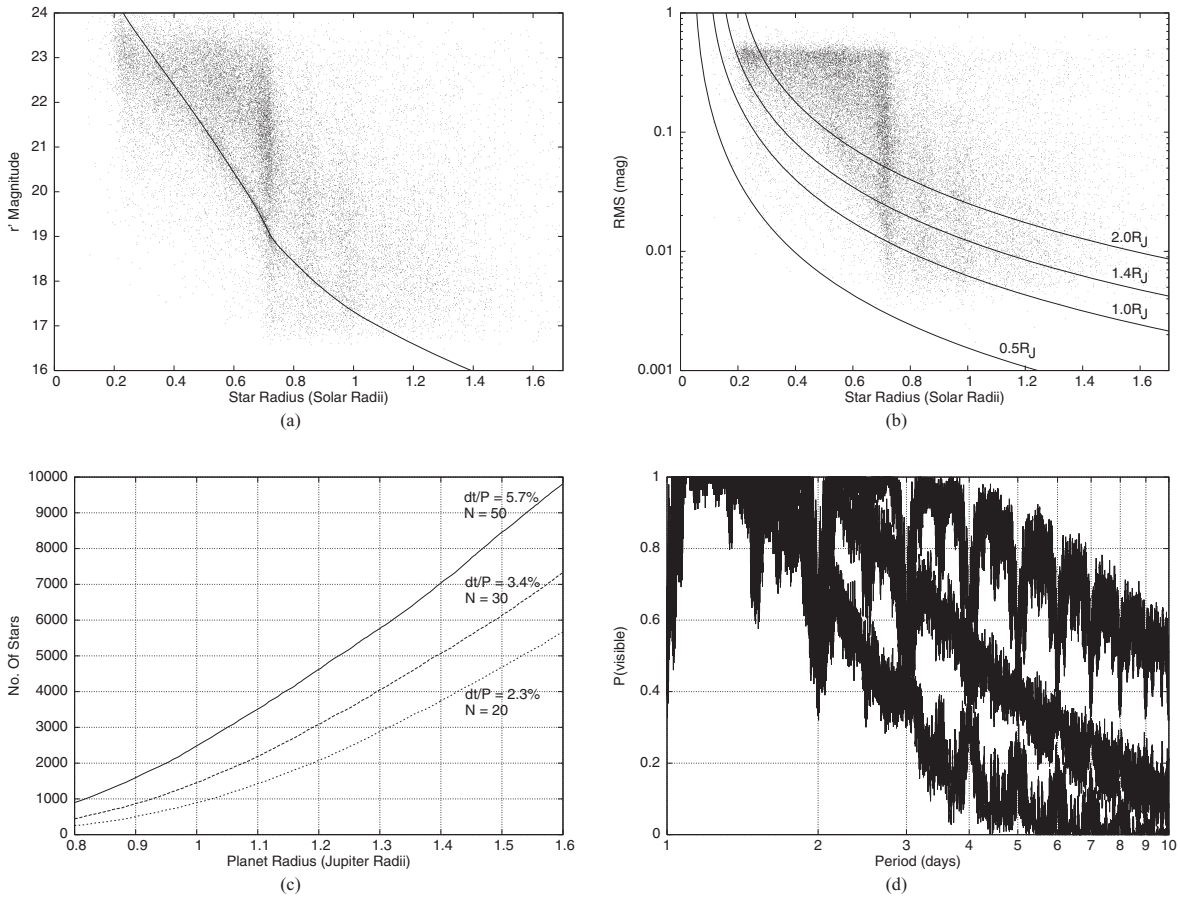


**Figure 3.** (a) A plot of $r'$ magnitude against star radius for all four chips. The continuous line is the theoretical cluster main sequence. (b) Standard deviation (rms) of the light curves against star radius for all four chips. The continuous curves are the detection limits for an HD 209458-like planet of the quoted radius as a function of star radius (see Section 4.5). (c) Number of stars in our survey that have an rms accuracy better than that required for a S/N $\approx 10$ detection with $N$ data points during transit as a function of planetary radius. (d) A plot of $P$(visible) against orbital period for $M = 1$ (upper curve), $M = 2$ (middle curve) and $M = 3$ (lower curve). $P$(visible) is the probability that at least $M$ transits have a time of mid-transit that occurs during our observations.

obtain these detection threshold curves, we note that the signal-to-noise ratio for detecting a transit is roughly

$$\mathrm{S/N} \approx \frac{\Delta m \sqrt{N}}{\sigma}, \tag{13}$$

where $\Delta m$ is the transit depth, $\sigma$ is the standard deviation of the photometric measurements, and $N$ is the number of data points acquired during the transit. The transit depth in magnitudes is approximately

$$\Delta m \approx -2.5 \log \left[ 1 - \left( \frac{R_\mathrm{p}}{R_*} \right)^2 \right], \tag{14}$$

where $R_\mathrm{p}$ is the radius of the planet and $R_*$ is the radius of the host star. For random sampling of the orbital period $P$, the probability that a given data point catches a transit is $\Delta t/P$, where $\Delta t$ is the transit duration. For an HD 209458b-like system ($\Delta m \approx 1.5$ per cent, $\Delta t \approx 3$ h, $P \approx 3.5$ d), this fraction is $\Delta t/P = 3.5$ per cent, and thus $N \sim 30$ of our 880 light-curve data points would catch a transit. For an OGLE-TR-56b-like system ($\Delta m \approx 1.3$ per cent, $\Delta t \approx 1.7$ h, $P \approx 1.2$ d), $\Delta t/P = 5.9$ per cent, and thus $N \sim 52$. In Section 5 we adopt a conservative transit detection threshold of S/N $\approx 10$. By rearranging equation (13) and using equation (14), we have plotted in Fig. 3(b) the required rms accuracy $\sigma$ to detect at S/N $= 10$ an HD 209458b-like system ($N = 30$) as a function of stellar radius $R_*$ for planetary radii of 0.5, 1.0, 1.4 and 2.0 $R_\mathrm{J}$.

In fact, we may count the number of stars in our survey that have an rms accuracy better than that required for a S/N $\approx 10$ detection with $N$ data points during transit. In Fig. 3(c) we plot this number against $R_\mathrm{p}$ for $N = 20$, 30 and 50. The curves $N = 30$ and $N = 50$ are representative of a typical hot Jupiter (HD 209458b) and a typical very hot Jupiter (OGLE-TR-56b), respectively. In Fig. 3(d) we plot $P$(visible) against orbital period, where $P$(visible) is the probability that at least $M$ transits have a time of mid-transit that occurs during our observations. The values $M = 1$, 2 and 3 are represented by the upper, middle and lower curves, respectively.

We may use Figs 3(c) and (d) to estimate the expected number of transiting planets. Assuming a typical hot Jupiter radius of 1.2 $R_\mathrm{J}$, then we estimate that there are 3083 and 4625 stars (Fig. 3c) whose light curves have sufficient accuracy in order to detect HD 209458b-like and OGLE-TR-56b-like planets respectively. Fig. 3(d) shows that 1–3 d planets are almost guaranteed to transit during our observations, and that 3–5 d planets have ∼80 per cent probability. Assuming that ∼1 per cent of stars host a hot Jupiter companion, and that ∼10 per cent of such systems exhibit transits, then we may expect ∼2 stars in our sample to reveal HD 209458b-like planetary transits or ∼4 stars in our sample to reveal OGLE-TR-56b-like planetary transits. In forthcoming work (Bramich & Horne, in preparation), we report results of more detailed modelling of the planet detection capabilities of our survey based on Monte Carlo simulations that are consistent with these results.

## 5 TRANSIT DETECTION

We used a matched filter algorithm to search for transits in the light curves. Adopting a square 'boxcar' shape for the transit light curve, the transit model has four parameters: the out-of-eclipse magnitude $m_0$, the time of mid-transit $t_0$, duration $\Delta t$, and depth $\Delta m$. We search for transits with durations ranging from 0.5 to 5 h, spanning this range with 12 values of $\Delta t$ spaced by factors of 1.23. We move the transit centroid $t_0$ through the data in steps of $\Delta t/4$. As illustrated in Fig. 4, we fit both a constant and a boxcar transit light curve to the data points in a window of width $5\Delta t$ centred on each value of $t_0$. Our transit detection statistic is

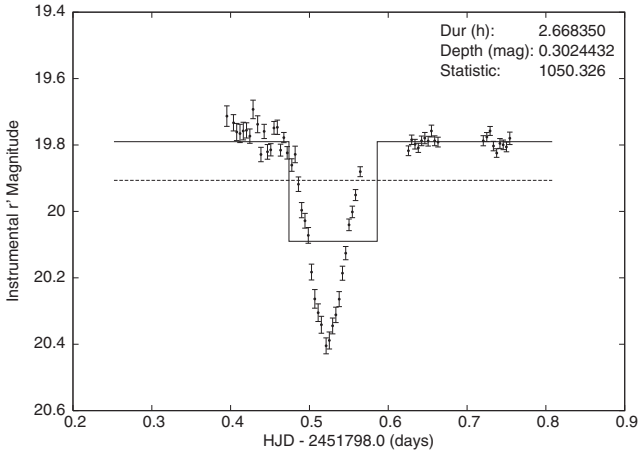


**Figure 4.** An example boxcar transit fit showing the in-transit and out-of-transit zones (continuous line) and the constant fit (dashed line). The horizontal axis is time (days) and the vertical axis instrumental Sloan $r'$ magnitude. 'Statistic' is the value of the transit statistic $S^2_\mathrm{tra}$ for this fit.

$$S^2_\mathrm{tra} \equiv \frac{\chi^2_\mathrm{const} - \chi^2_\mathrm{tra}}{\chi^2_\mathrm{out}/(N_\mathrm{out} - 1)}, \tag{15}$$

where $\chi^2_\mathrm{tra}$ is the chi-squared value of the boxcar transit fit, $\chi^2_\mathrm{const}$ is the chi-squared value of the constant fit, and $\chi^2_\mathrm{out}$ is the chi-squared value of the boxcar transit fit for the $N_\mathrm{out}$ out-of-transit data points. The statistic $S^2_\mathrm{tra}$ is effectively the squared signal-to-noise ratio of the fitted transit signal renormalized to the reduced chi-squared of the out-of-transit data points. This modified matched filter algorithm was designed to help down-weight systematic errors with $\chi^2_\mathrm{out}/(N_\mathrm{out} - 1) > 1$ (and, serendipitously, variables), since transit signals should have $\chi^2_\mathrm{out}/(N_\mathrm{out} - 1) \sim 1$.

The transit detection algorithm outlined above was applied to the 1999–07 and 2000–09 runs. Initial tests with $S^2_\mathrm{tra}$ generated many spurious transit candidates in which the transit fit matched low data points at the beginning or end of a night. To suppress these, we introduced additional requirements on the number of in-transit and out-of-transit light-curve data points. For the densely sampled 2000–09 run, we required at least three in-transit and eight out-of-transit light-curve data points for a transit detection. For the more sparsely sampled 1999–07 run, we required at least two in-transit and six out-of-transit light-curve data points for a transit detection. The time sampling in the 1999–06 run was too sparse to support transit hunting via the above technique.

In each light curve the highest value of $S^2_\mathrm{tra}$ on each night was identified, and those with $S^2_\mathrm{tra} \geqslant 100$ (equivalent to S/N $\geqslant 10$) were retained for closer examination. Table 5 lists for each chip the number of raw candidate transits thereby selected over the two runs.

**Table 5.** Number of raw transit candidates and remaining transit candidate light curves after the weeding process for each chip over the two runs.

| Chip No. | No. raw transit candidates | No. remaining transit candidate light curves |
|---|---|---|
| 1 | 617 | 9 |
| 2 | 311 | 5 |
| 3 | 721 | 6 |
| 4 | 533 | 4 |
| Total | 2182 | 24 |

Despite the high signal-to-noise ratio threshold for detection, 2182 raw transit candidates were found. A careful visual inspection of the corresponding light curves led us to reject the majority of these based on a number of criteria. The majority of the raw transit candidates (61.8 per cent) were rejected because they appeared to represent a single much fainter data point resulting from a 'bad' section in one of the difference images. Such cases were readily identifiable because the light curves of many stars triggered a transit detection at the same epoch. A large number of variable stars were picked up ($\sim$100 light curves, $\equiv$19.5 per cent of the raw transit candidates), which we plan to present in a forthcoming paper. Light curves showing eclipses with clearly different depths were also assigned as variable stars since a stellar binary is indicated in this case.

For the remaining raw transit candidates, we examined the star on the reference frame. This revealed that many of the remaining transit signatures were caused by the following (in order of most common occurrence):

(i) image defects detected as 'stars' (4.5 per cent);
(ii) stars lying on or close to image defects, bad columns and/or saturation spikes (4.0 per cent);
(iii) stars close to saturation (3.7 per cent);
(iv) very closely blended stars (2.1 per cent);
(v) stars close to the edge of the CCD (0.8 per cent).

The reference image for each chip contained a large number of saturated stars along with large saturation spikes, which unfortunately increased the incidence of such false alarms.

For the transit candidate light curves that survived to this point, we checked the difference images for the night(s) of the suspected transit(s) by constructing a difference image movie. This revealed that a handful of the candidates (0.6 per cent) were the result of a consecutive set of poor subtractions at the star position. The other candidates clearly showed a flat difference image followed by a growing and then diminishing 'dimple', indicating a drop and then recovery in the brightness of the star.

We discuss in Section 6 below the 24 transit candidate light curves that passed all of the data quality tests outlined above. Reference to a transit candidate from now on refers only to one of these transit candidate light curves. Fig. 5 shows all tests for which $S^2_{\rm tra} \geqslant 10$ and highlights the eclipse with the greatest value of $S^2_{\rm tra}$ for each transit candidate. Table 6 details the number of fully and partially observed eclipses that are present for each transit candidate and how these eclipses are distributed between the three runs. Table 6 also lists the J2000.0 celestial coordinates for each transit candidate.

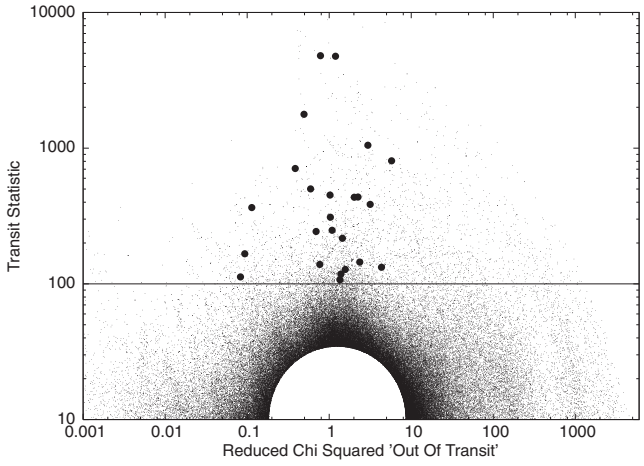


**Figure 5.** The transit detection statistic $S^2_{\rm tra}$ against the out-of-transit reduced chi-squared $\chi^2_{\rm out}/(N_{\rm out} - 1)$. The initial transit detection threshold shown by the horizontal line is set at $S^2_{\rm tra} = 100$. The strongest transits detected in the light curves of the 24 stars that survived subsequent data quality tests are plotted as solid circles. The blank semicircular region is saturated with test points.

## 6 TRANSIT CANDIDATES

### 6.1 Theoretical models

The light curves of the 24 transit candidates selected in Section 5 were modelled as a star and planet system in the following way. We assume spherical stars, a luminous primary of radius $R_*$ and a dark massless companion of radius $R_{\rm c}$ in a circular orbit with radius $a$ and period $P$ inclined by the inclination $i$ relative to our line of sight. The time $t_0$ is the time of mid-eclipse of the primary by the companion. Since we already know $R_*$, the parameters that need to be constrained for such a system are $P$, $t_0$, $i$, $R_{\rm c}$ and a constant magnitude $m_0$. Periodic variations in the apparent brightness of the star were also accounted for in three different ways, leading to three competing planetary transit models.

Model 1:

$$f_1(t) = f_0[1 - f_{\rm c}(t)]. \tag{16a}$$

Model 2:

$$f_2(t) = f_1(t)\left[1 + A\sin\left(\frac{2\pi(t - t_0)}{P_{\rm var}} + \phi\right)\right]. \tag{16b}$$

Model 3:

$$f_3(t) = f_1(t)\left[1 - C_{\rm e}\cos\left(\frac{4\pi(t - t_0)}{P}\right) - C_{\rm h}\cos\left(\frac{2\pi(t - t_0)}{P}\right)\right]. \tag{16c}$$

The function $f_n(t)$ is the predicted stellar flux at time $t$ for model $n$, $f_0$ is a constant flux value and $f_{\rm c}(t)$ is the fraction of the total stellar flux obscured by the companion at time $t$. The function $f_1(t)$ is calculated in a numerical fashion by creating a grid for the observed stellar disc and calculating the flux from each grid element taking into account the apparent position of the companion at time $t$ and the effect of linear limb darkening with $u = 0.5$.

Model 1 is therefore appropriate for a star with a constant brightness. Model 2 incorporates sinusoidal stellar flux variations of semi-amplitude $A$ and phase $\phi$, which do not necessarily have the same period as the orbital period of the companion. Such variations may be present for stars with a lot of starspot activity. Model 3 incorporates stellar flux variations due to two effects. The first effect, modelled by the $C_{\rm e}$ cosine term, is due to the star being tidally distorted into an ellipsoidal shape by the companion and rotationally synchronized. The value of $C_{\rm e}$ quantifies the semi-amplitude of such ellipsoidal flux variations. The second effect, modelled by the $C_{\rm h}$ cosine term, is due to heating on one side of the companion caused by irradiation by the star. The value of $C_{\rm h}$ quantifies the semi-amplitude of the heating term.

If stellar flux variations exist, and they are best modelled by ellipsoidal and/or heating terms, then this favours a stellar rather than a planetary companion. A planet does not have enough mass to distort the shape of the star, and neither does a planet emit enough radiation to be detectable in the light curve. Eclipses with different depths also imply a stellar companion, since the secondary eclipse

**Table 6.** Star and light-curve properties for the transit candidates. The numbers in parentheses indicate the uncertainty on the last decimal place. Columns 2 and 3 are calibrated $r'$ and $r' - i'$ using the shifts in Table 4. Columns 7–9 indicate the number of fully and partially observed eclipses '(f, p)' that are present in the light curve of the corresponding run. The eclipsing stellar binaries are classified into the following categories: E = eclipsing binary; EA = Algol-type eclipsing binary; RS = RS Canum Venaticorum-type eclipsing binary; CV = cataclysmic variable.

| Star | $r'$ (mag) | $r' - i'$ (mag) | Mass ($M_\odot$) | Radius ($R_\odot$) | Distance (pc) | 1999–06 f, p | 1999–07 f, p | 2000–09 f, p | RA (J2000.0) | Dec. (J2000.0) | Variable class |
|---|---|---|---|---|---|---|---|---|---|---|---|
| EB-1 | 18.077 | 0.569(17) | 0.949(33) | 0.947(42) | 2908(13) | 0, 0 | 0, 1 | 0, 0 | 23 58 36.75 | +56 26 56.1 | E |
| EB-2 | 19.140 | 0.538(9) | 1.028(22) | 1.062(35) | 5762(11) | 0, 0 | 0, 1 | 0, 2 | 23 58 33.88 | +56 37 04.9 | E |
| EB-3 | 19.346 | 0.606(12)[a] | 0.897(23) | 0.882(29) | 4346(31) | 0, 0 | 0, 1 | 0, 1 | 23 57 11.92 | +56 31 24.9 | RS |
| EB-4 | 19.447 | 0.999(10) | 0.666(4) | 0.635(4) | 1799(4) | 0, 0 | 0, 0 | 0, 1 | 23 56 46.79 | +56 36 13.8 | E |
| EB-5 | 20.088 | 0.773(18)[a] | 0.751(5) | 0.716(5) | 3564(20) | 0, 0 | 1, 1 | 1, 1 | 23 55 58.93 | +56 40 29.6 | E |
| EB-6 | 17.338 | 0.695(45) | 0.759(23) | 0.723(24) | 1168(2) | 0, 1 | 0, 1 | 0, 1 | 23 55 42.99 | +56 39 14.9 | E |
| EB-7 | 20.865 | 0.560(37) | 0.98(8) | 1.00(13) | 11312(52) | 0, 0 | 1, 0 | 1, 0 | 23 58 27.34 | +56 46 36.4 | E |
| EB-8 | 18.900 | 0.788(9)[a] | 0.740(3) | 0.707(3) | 2037(39) | 0, 5 | 2, 3 | 5, 2 | 23 58 29.19 | +56 32 42.7 | RS |
| EB-9 | 19.981 | 0.925(12)[a] | 0.701(4) | 0.671(4) | 2647(51) | 1, 2 | 3, 1 | 5, 2 | 23 55 18.41 | +56 43 14.3 | RS |
| EB-10 | 20.323 | 1.025(19)[b] | 0.662(8) | 0.630(8) | 2545(79) | 0, 0 | 1, 1 | 3, 2 | 23 57 29.99 | +56 57 34.3 | RS |
| EB-11 | 20.402 | 0.616(24) | 0.89(5) | 0.87(6) | 6784(22) | 0, 0 | 0, 0 | 3, 2 | 23 58 13.37 | +56 45 36.1 | E |
| EB-12 | 16.724 | 0.55(8)[b] | 0.94(17) | 0.93(25) | 1589(17) | 0, 1 | 1, 2 | 0, 0 | 23 57 12.86 | +56 31 26.5 | EA |
| EB-13 | 19.728 | 0.562(13)[a] | 0.980(23) | 0.988(34) | 6619(59) | 1, 1 | 3, 0 | 2, 1 | 23 55 59.17 | +56 45 14.1 | EA |
| EB-14 | 17.571 | 0.427(10)[a] | 1.33(4) | 1.57(7) | 5599(85) | 0, 3 | 1, 2 | 3, 1 | 23 57 18.04 | +56 51 12.0 | EA |
| EB-15 | 20.619 | 1.133(18)[a] | 0.620(9) | 0.586(10) | 2378(133) | 1, 1 | 2, 2 | 5, 1 | 23 58 39.38 | +56 36 44.7 | RS or CV |
| EB-16 | 21.120 | 1.853(19) | 0.239(6) | 0.245(4) | 752(4) | 0, 1 | 1, 0 | 1, 1 | 23 56 57.23 | +56 34 03.4 | E |
| EB-17 | 19.420 | 1.298(9)[a] | 0.544(5) | 0.507(4) | 1043(14) | 1, 0 | 2, 0 | 2, 0 | 23 56 47.64 | +56 36 28.7 | RS |
| EB-18 | 17.650 | 0.64(9)[a] | 0.81(12) | 0.78(14) | 1578(10) | 0, 0 | 0, 1 | 0, 2 | 23 56 01.68 | +56 43 08.3 | RS |
| EB-19 | 17.368 | 0.62(7) | 0.82(10) | 0.79(12) | 1477(2) | 0, 1 | 0, 1 | 0, 2 | 23 56 36.67 | +56 52 43.4 | RS |
| EB-20 | 20.080 | 0.797(18)[a] | 0.743(6) | 0.710(5) | 3423(84) | 0, 0 | 1, 0 | 2, 1 | 23 56 11.77 | +56 45 55.6 | RS |
| EB-21 | 18.984 | 1.516(9) | 0.399(6) | 0.379(5) | 526(2) | 0, 1 | 0, 0 | 1, 0 | 23 57 51.16 | +56 42 03.2 | E |
| TR-1 | 20.703 | 0.632(32) | 0.87(5) | 0.84(6) | 7291(30) | 0, 0 | 0, 1 | 1, 0 | 23 57 45.06 | +56 55 36.6 | |
| TR-2 | 18.024 | 0.467(8) | 1.195(22) | 1.348(37) | 5348(7) | 0, 0 | 0, 0 | 1, 0 | 23 57 24.52 | +56 55 17.6 | |
| TR-3 | 19.553 | 0.971(9) | 0.679(4) | 0.649(4) | 1995(5) | 1, 0 | 0, 0 | 2, 1 | 23 56 47.11 | +56 51 10.2 | |

Notes. [a]Colour-corrected using the light-curve model. [b]Colour-corrected using interpolation of the light curve.

is caused by occultation of the companion, indicating that the companion is emitting enough radiation to contribute to the observed brightness of the system.

In the following sections, the transit candidates have been organized into groups depending on the light-curve properties, and analysed accordingly. Relevant parameters are shown on the light-curve plots. Periods were initially determined using a periodogram, and then refined during the fitting of the appropriate transit model. We refer to any transit fit for which all five parameters have been optimized as a 'full transit fit'. For brevity, the following labelling format has been adopted for the plots in these sections:

⟨Star No.⟩ – ⟨Plot code⟩ – ⟨Run(s) to which plot applies⟩

The plot codes are as follows:

| | |
|---|---|
| L, | light curve |
| PL, | phased light curve |
| CPL, | close-up of phased light curve |
| BL, | binned light curve |
| CTFIT, | central transit fit |
| FTFIT, | full transit fit |
| CM, | chi-squared contour map showing the best-fitting solution with a cross and the 1, 2 and 3$\sigma$ confidence regions with solid, dashed and short dashed lines, respectively; annular, grazing and no eclipse regions are separated by thick solid lines. |

### 6.2 Eclipsing binaries with undetermined periods

In Fig. 6 we present seven transit candidates for which we were unable to determine a period, although we were able to classify them as eclipsing binaries. The reason for not being able to determine the period was due to either the presence of only one fully/partially observed eclipse in the light curve and/or cycle ambiguity between eclipses. We fitted the best-defined eclipse for each candidate with model 1, keeping the inclination fixed at 90.0° (we call this a 'central transit fit'). This fit determines a minimum radius of the companion given the eclipse profile, since at lower inclination values the same size companion obscures a smaller fraction of the total stellar flux due to limb-darkening effects and the possibility that the eclipse is grazing instead of annular. Hence, at lower inclinations, a larger companion radius is required to account for the observed eclipse depth.

For each of the seven transit candidates except EB-3, the central transit fit yields a minimum companion radius that is greater than 0.2 $R_\odot$. This favours a stellar rather than a planetary companion. The lack of out-of-eclipse light-curve variations leads us to conclude that these are eclipsing binaries. For EB-2, a periodogram reveals that there are only two possible periods (3.6216 ± 0.0053 d and 7.233 ± 0.010 d). We plot the 2000–09 light curve folded on the shorter period in Fig. 6(b).

In the case of EB-3, the derived minimum companion radius of 0.18 $R_\odot$ is most likely to be an underestimate since the eclipse is possibly deeper than the fit shown in Fig. 6(f). Also, the light curve

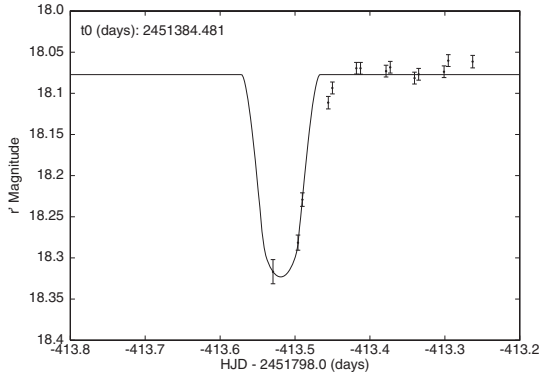


(a) **EB-1** - L & CTFIT - 1999-07 Night 3

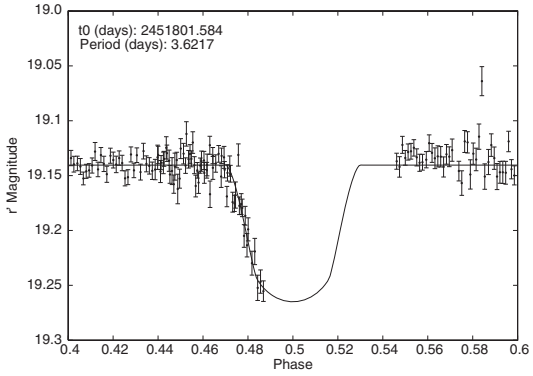


(b) **EB-2** - CPL & CTFIT - 2000-09

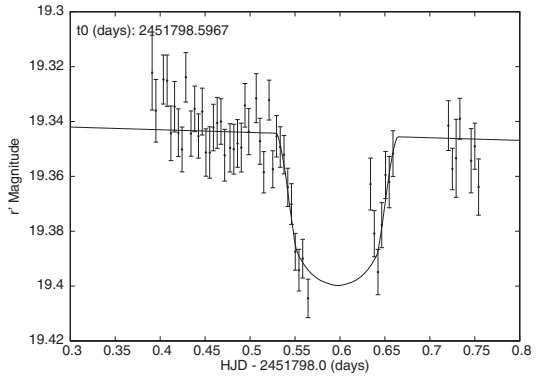


(c) **EB-3** - L & CTFIT - 2000-09 Night 1

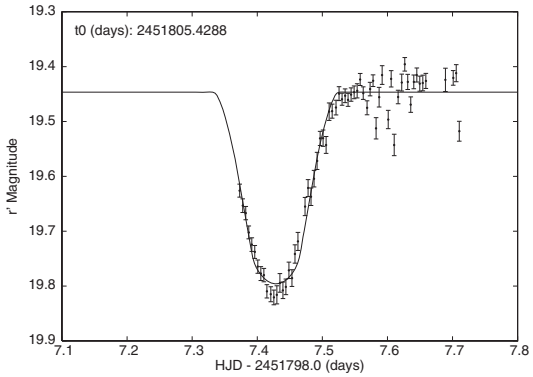


(d) **EB-4** - L & CTFIT - 2000-09 Night 8

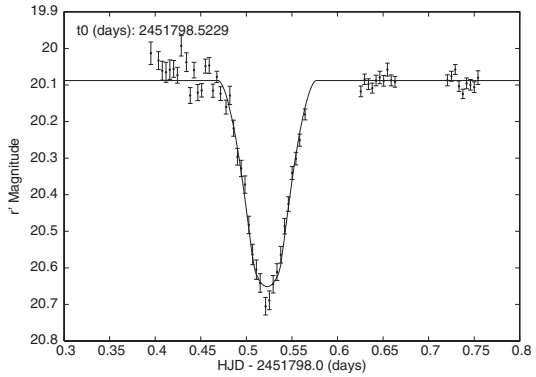


(e) **EB-5** - L & CTFIT - 2000-09 Night 1

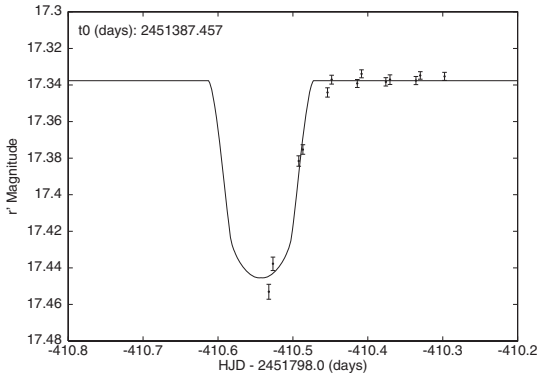


(f) **EB-6** - L & CTFIT - 1999-07 Night 6

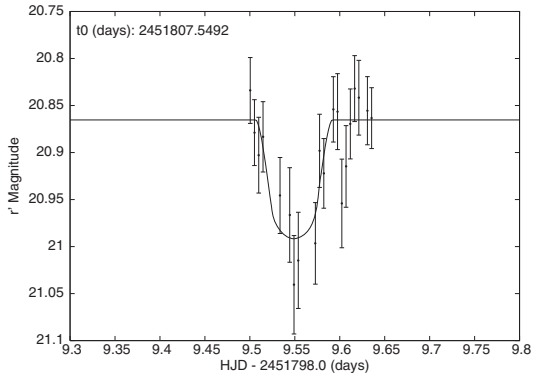


(g) **EB-7** - L & CTFIT - 2000-09 Night 10

**Figure 6.** Eclipsing binaries with undetermined periods.

shows sinusoidal out-of-eclipse variations. Therefore, we class this system as a RS CVn-type eclipsing binary.

### 6.3 Eclipsing binaries exhibiting secondary eclipses

In Fig. 7 we present four transit candidates that exhibit secondary eclipses in their light curves, implying that the companion is luminous. Fig. 7 shows the folded light curve for each transit candidate along with the best-fitting transiting planet model. The light curves from the different runs are offset vertically (in magnitude) from each other in order to highlight any changes in the out-of-eclipse variations.

### 6.4 Eclipsing binaries exhibiting ellipsoidal variations and heating effects

In Fig. 8 we present three transit candidates that exhibit ellipsoidal variations and heating effects in their light curves, which immediately implies that the companion is stellar. Fig. 8 shows the folded light curve for each transit candidate along with the best-fitting transiting planet model using model 3. The light curves from different runs are offset vertically (in magnitude) from each other in order to highlight any changes in the amplitude of the out-of-eclipse variations.

### 6.5 A possible long-period cataclysmic variable

EB-15 is a 10.8-h eclipsing binary (Fig. 9) that has round-bottomed eclipses lasting 0.1 in phase and orbital modulations that peak near phase 0.2. With $r' \approx 20.62$ mag and $r' - i' \approx 1.13$ mag, the star falls close to the cluster main sequence (Fig. 2a). The colour index is consistent with a $0.62\,M_{\odot}$ K7V star at $d = 2.4$ kpc, a possible cluster member. Over the three runs the orbital modulations increase in amplitude from 0.1 mag to 0.2 mag, while the eclipse depth decreases from 0.40 mag to 0.24 mag.

The orbital modulation could arise from spots on one or both stars, though this would require a preferred longitude that remains stable over 15 months. The orbital phasing is consistent with that of an 'orbital hump' that is often seen in quiescent dwarf novae, arising from the anisotropic emission of a 'hotspot' on the rim of an accretion disc where the mass transfer stream from the companion star feeds material into the disc. The relatively shallow eclipse would then imply a moderate inclination so that the donor star eclipses only the near rim of the disc and possibly the hotspot. The eclipse shape is more symmetric than would be expected for eclipses of a hotspot, however, and a hotspot eclipse would become deeper rather than shallower as the orbital modulation increased. We are unable to decide which interpretation may be correct, and recommend follow-up observations to resolve this ambiguity. In any case the eclipse is too deep to be attributed to a planetary transit.

### 6.6 More eclipsing binaries

In this section we present six transit candidates exhibiting neither easily discernible secondary eclipses nor orbital modulations consistent with ellipsoidal variations and heating effects. Figs 10 and

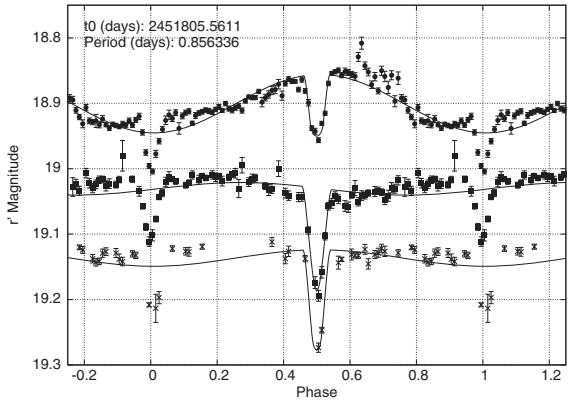


(a) **EB-8** - PL, BL & FTFIT - 2000-09 (Top), 1999-07 (Middle with +0.1 mag offset) & 1999-06 (Bottom with +0.2 mag offset)

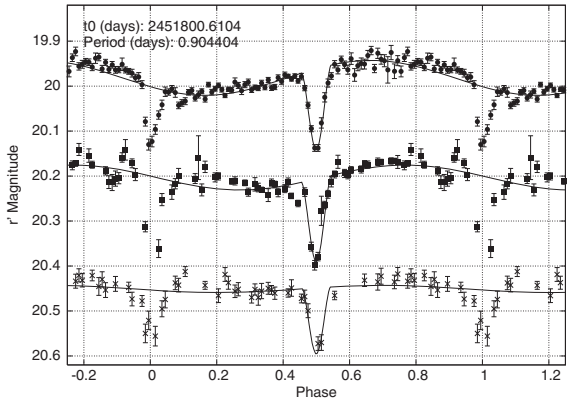


(b) **EB-9** - PL, BL & FTFIT - 2000-09 (Top), 1999-07 (Middle with +0.2 mag offset) & 1999-06 (Bottom with +0.4 mag offset)

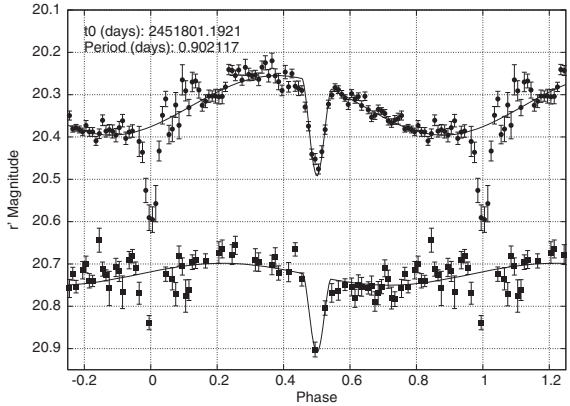


(c) **EB-10** - PL, BL & FTFIT - 2000-09 (Top) & 1999-07 (Bottom with +0.4 mag offset)

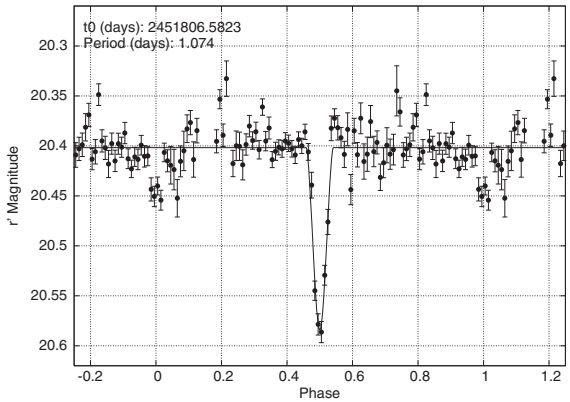


(d) **EB-11** - PL, BL & FTFIT - 2000-09

**Figure 7.** Eclipsing binaries exhibiting secondary eclipses.

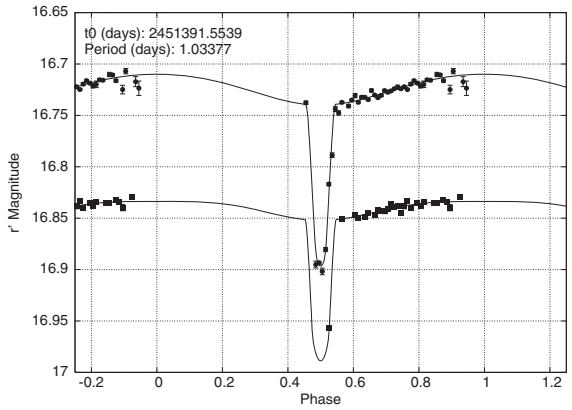


(a) **EB-12** - PL, BL & FTFIT - 1999-07 (Top) & 1999-06 (Bottom with +0.1 mag offset)

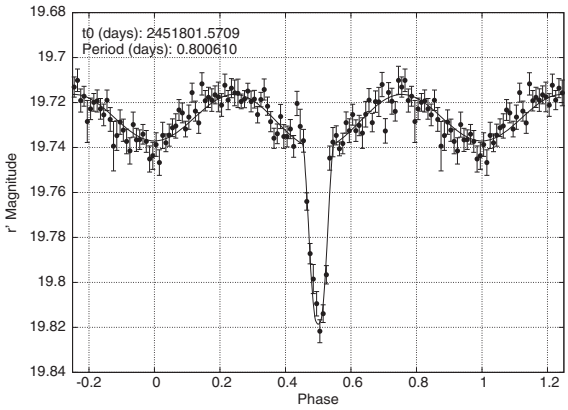


(b) **EB-13** - PL, BL & FTFIT - 1999-06, 1999-07 & 2000-09

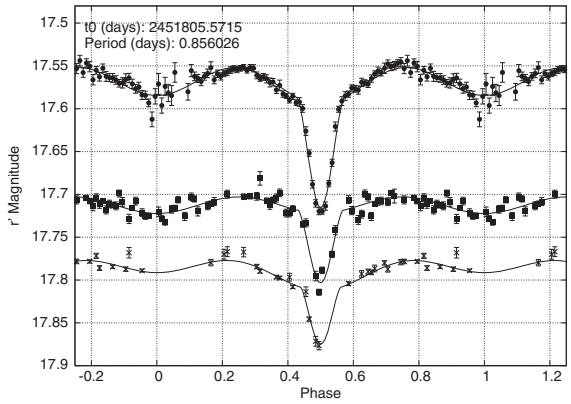


(c) **EB-14** - PL, BL & FTFIT - 2000-09 (Top), 1999-07 (Middle with +0.1 mag offset) & 1999-06 (Bottom with +0.2 mag offset)

**Figure 8.** Eclipsing binaries exhibiting ellipsoidal variations and heating effects.

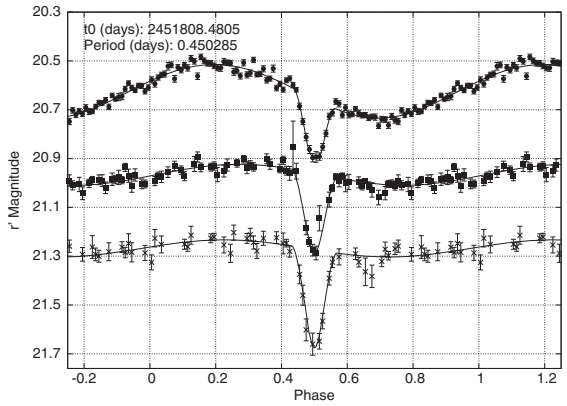


(a) **EB-15** - PL, BL & FTFIT - 2000-09 (Top), 1999-07 (Middle with +0.3 mag offset) & 1999-06 (Bottom with +0.6 mag offset)

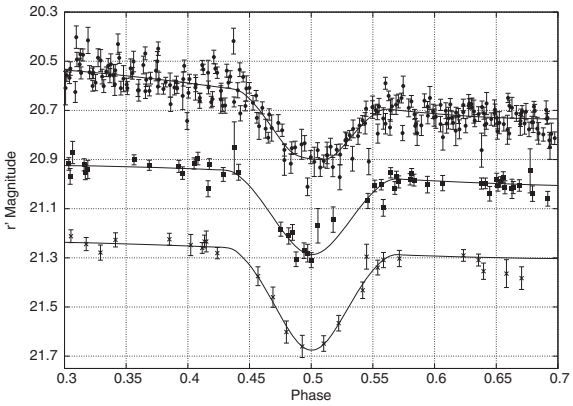


(b) **EB-15** - CPL & FTFIT - 2000-09 (Top), 1999-07 (Middle with +0.3 mag offset) & 1999-06 (Bottom with +0.6 mag offset)

**Figure 9.** Possible long-period cataclysmic variables.

11 show for each star a folded and binned light curve with the best-fitting transiting planet model, and an unbinned close-up of the folded light curve around the primary eclipse along with the best-fitting model. For EB-17 the light curves from different runs are offset vertically to highlight changes in the amplitude and phase of the out-of-eclipse variations. We rule out the transiting planet model for stars EB-16 to EB-20 because the full transit fit yields a companion radius greater than $0.2\,\mathrm{R}_{\odot}$. For EB-21 the full transit fit admits $R_{\mathrm{c}} < 0.2\,R_{\odot}$ but only for periods $P < 1.1$ d that are ruled out, and hence the transiting planet model is ruled out also for EB-21.

EB-16 is an interesting case in its own right. The light curve shows four V-shaped eclipses of depth 0.39 mag and duration 1.3 h over the three runs. Figs 10(a) and (b) show the light curve folded

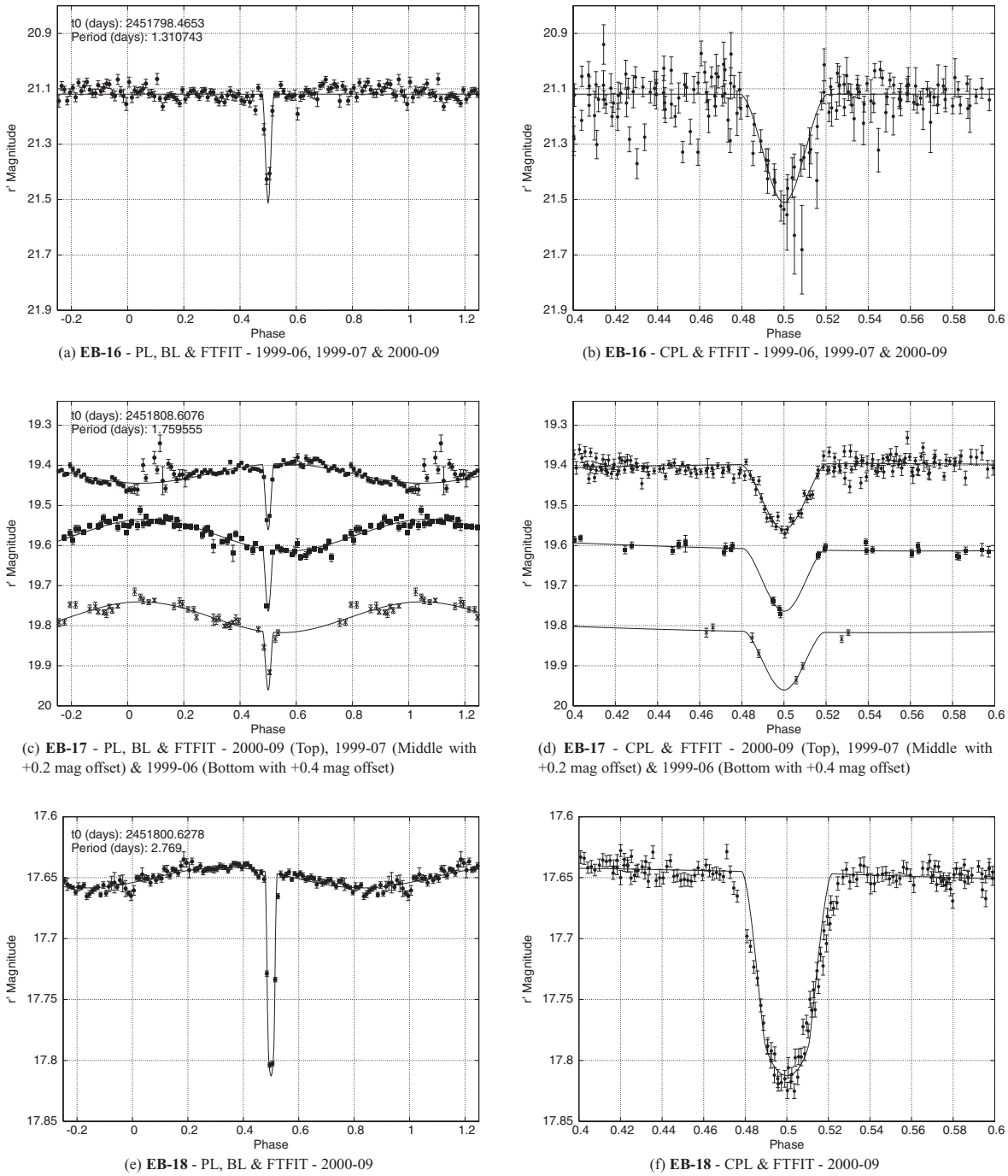


(a) **EB-16** - PL, BL & FTFIT - 1999-06, 1999-07 & 2000-09

(b) **EB-16** - CPL & FTFIT - 1999-06, 1999-07 & 2000-09

(c) **EB-17** - PL, BL & FTFIT - 2000-09 (Top), 1999-07 (Middle with +0.2 mag offset) & 1999-06 (Bottom with +0.4 mag offset)

(d) **EB-17** - CPL & FTFIT - 2000-09 (Top), 1999-07 (Middle with +0.2 mag offset) & 1999-06 (Bottom with +0.4 mag offset)

(e) **EB-18** - PL, BL & FTFIT - 2000-09

(f) **EB-18** - CPL & FTFIT - 2000-09

**Figure 10.** EB-16, EB-17 and EB-18.

on the 1.31-d period. With $r' \approx 21.12$ mag and $r' - i' \approx 1.85$ mag, we derive a primary $0.24\,M_{\odot}$ M5V star at $d \sim 750$ pc, in front of the cluster. The full transit fit reveals that the companion is the same size as the primary at $0.245\,R_{\odot}$ and that the eclipses are grazing. Hence the period is actually 2.62 d and we classify the system as a grazing eclipsing binary consisting of a pair of M5V stars, an interesting discovery in that few such systems are known.

EB-21 is a difficult case in that the light-curve data show one eclipse in the 1999–06 run with only two data points during the eclipse, and one well-sampled eclipse in the 2000–09 run (Fig. 11f). The eclipse is V-shaped of depth 0.2 mag and duration 1.0 h, suggesting that it is likely to be a grazing eclipse. With $r' \approx 18.98$ mag and $r' - i' \approx 1.52$ mag, we find that the primary is a $0.40\,M_{\odot}$ M2V star that lies at only ∼530 pc. A central transit fit to the 2000–09 data (Fig. 11f) yields a minimum companion radius of $0.141\,R_{\odot}$ because of the small size of the primary star ($0.38\,R_{\odot}$), from which we cannot rule out the transiting planet model. Analysis of the shape of the single eclipse in the 2000–09 data is possible due to the good time sampling of the observations, and such an analysis may reveal whether the eclipse is the result of an annular occultation by a smaller companion or a grazing occultation by a larger companion. Also, we may attempt to predict the orbital period $P$ of the planetary companion as a function of the impact parameter $b = a \cos i / R_*$ of the eclipse and subsequently use the light-curve data from the whole

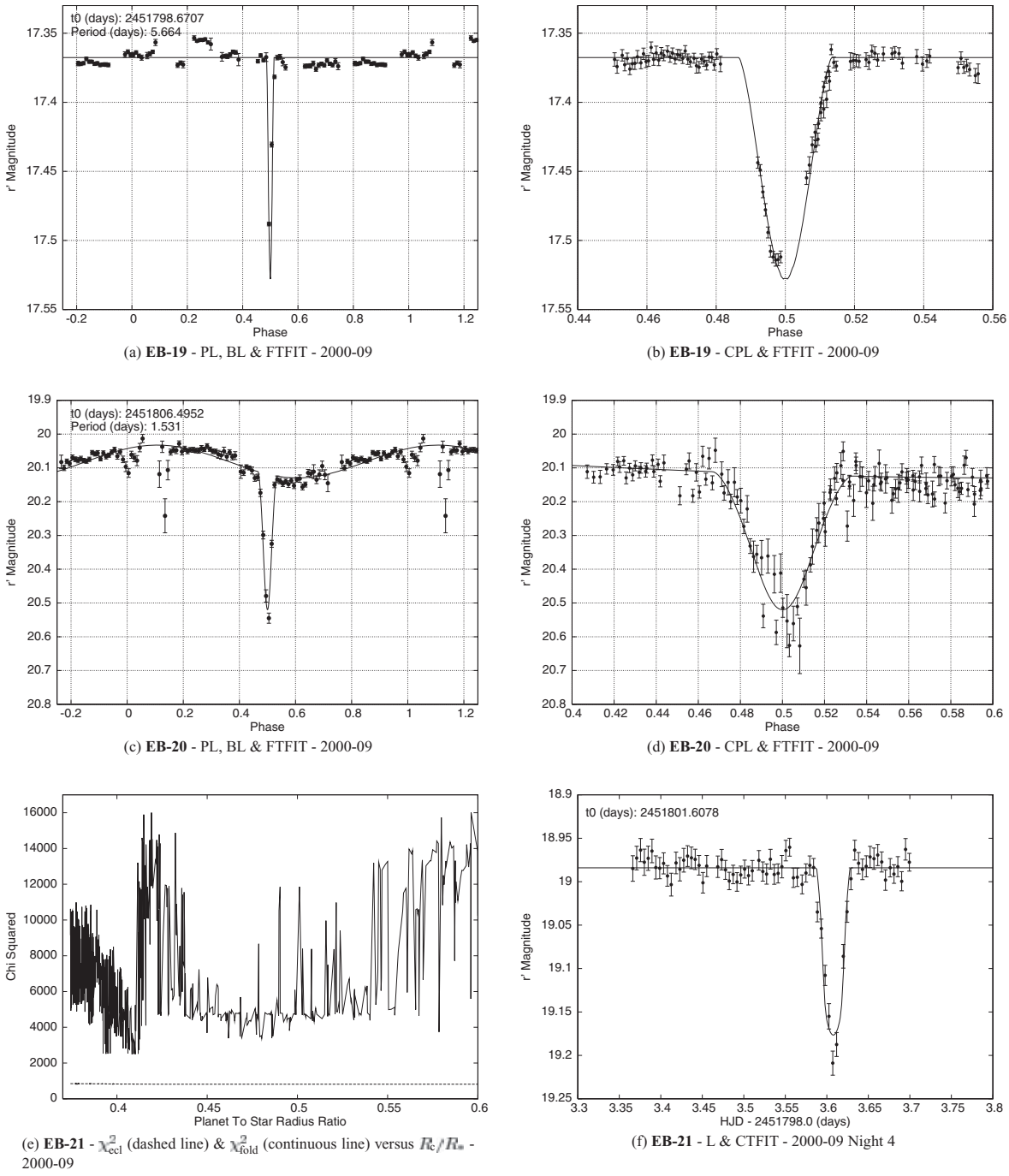


(a) **EB-19** - PL, BL & FTFIT - 2000-09

(b) **EB-19** - CPL & FTFIT - 2000-09

(c) **EB-20** - PL, BL & FTFIT - 2000-09

(d) **EB-20** - CPL & FTFIT - 2000-09

(e) **EB-21** - $\chi^2_{\rm ecl}$ (dashed line) & $\chi^2_{\rm fold}$ (continuous line) versus $R_{\rm c}/R_*$ - 2000-09

(f) **EB-21** - L & CTFIT - 2000-09 Night 4

**Figure 11.** EB-19, EB-20 and EB-21.

run to determine which periods, and hence which values of $b$, may be ruled out.

For EB-21 we created a grid for the impact parameter $b$ from 0.0 to 1.0. For each value of $b$ we fitted model 1 to the single eclipse in the 2000–09 run, using the light-curve data from the whole run, in order to determine a time of mid-transit $t_0$, a constant magnitude $m_0$, a planetary radius $R_{\rm c}$ and a transit duration $\Delta t$. The chi-squared $\chi^2_{\rm ecl}$ of the fit was also calculated. The duration of a transit event is given by

$$\Delta t = \frac{P R_*}{\pi a}\sqrt{\left(1+\frac{R_{\rm c}}{R_*}\right)^2 - b^2}. \tag{17}$$

We also have Kepler's third law,

$$P^2 = \frac{4\pi^2 a^3}{G M_*}. \tag{18}$$

We already know $M_*$ and $R_*$, and since we have $R_{\rm c}$ and $\Delta t$ as functions of $b$ from our fits of the single eclipse, we may use equations (17) and (18) to estimate $P$ (or $a$) as a function of $b$ for the transiting planet model. For each value of $b$ we folded the 2000–09 light curve of EB-21 on the predicted period $P$ using the fitted $t_0$, and calculated a new chi-squared $\chi^2_{\rm fold}$ using the fit to the single eclipse with period $P$. In general, if the predicted period is such that none of the folded light-curve data fall during the eclipse, then $\chi^2_{\rm fold} = \chi^2_{\rm ecl}$. However, if the predicted period is such that some of the folded light-curve data

do fall during the eclipse, then $\chi^2_{\rm fold} \gg \chi^2_{\rm ecl}$, ruling out that particular period, impact parameter and corresponding eclipse solution.

Fig. 11(e) shows a plot of $\chi^2_{\rm ecl}$ versus $R_{\rm c}/R_*$ (dashed line), which appears constant because of the scale on the *y*-axis. The continuous line is a plot of $\chi^2_{\rm fold}$ versus $R_{\rm c}/R_*$, which clearly shows that $\chi^2_{\rm fold} \gg \chi^2_{\rm ecl}$ for all values of $R_{\rm c}$ from 0.141 $R_\odot$ (the minimum companion radius with $b = 0$ and $R_{\rm c}/R_* = 0.373$) to 0.227 $R_\odot$ ($b = 0.92$ and $R_{\rm c}/R_* = 0.600$). This is due to the fact that the predicted period is less than 1.10 d for these values of $b$. This demonstrates that the transiting planet model is inconsistent with our observational data for this star, and hence a stellar companion is favoured. We have classified this system as an eclipsing binary.

### 6.7 INT-7789-TR-1

TR-1 exhibits one poorly sampled partially observed eclipse during the 1999–07 run and one well-sampled fully observed eclipse of depth 0.07 mag and duration 6.0 h in the 2000–09 run (Fig. 12b), and as a result we were unable to determine a period for the system. The star has $r' \approx 20.70$ mag and $r' - i' \approx 0.63$ mag, from which we derive a 0.87 $M_\odot$ late G star primary that lies far behind the cluster ($d = 7.3$ kpc). A central transit fit to the 2000–09 data yields a minimum companion radius of 0.188 $R_\odot$, from which we cannot rule out the transiting planet model.

Analysing the single eclipse in the 2000–09 run using the same method as for EB-21 in Section 6.6 yields a predicted period of 7.0 d for $b = 0$ that increases rapidly with increasing values of $b$. In fact $\chi^2_{\rm fold} = \chi^2_{\rm ecl}$ for all $b > 0.09$. Fig. 12(a) shows a plot of $\chi^2_{\rm ecl}$ versus $R_{\rm c}/R_*$ (dashed line) for $b = 0$ ($R_{\rm c}/R_* = 0.223$) to $b = 1.13$ ($R_{\rm c}/R_* = 0.500$). The minimum value of $\chi^2_{\rm ecl}$ obtained is $\chi^2_{\rm ecl} = 925.0$ corresponding to $R_{\rm c}/R_* = 0.500$, and this is marked on Fig. 12(a) as a horizontal shorter dashed line, along with the chi-squared values $\chi^2_{\rm ecl} = 925.0{+}1.0$ and $\chi^2_{\rm ecl} = 925.0{+}4.0$ corresponding to the $1\sigma$ and $2\sigma$ confidence levels.

One can see from Fig. 12(a) that $R_{\rm c}/R_* \geqslant 0.243$ with a $1\sigma$ confidence. This is equivalent to stating that $R_{\rm c} \geqslant 0.205\,R_\odot$ with a $1\sigma$ confidence. As a result, we can only rule out the transiting planet model for this transit candidate at the $1\sigma$ level, and therefore further observations are required to confirm the conclusion that this system is an eclipsing binary. Fig. 12(b) shows a plot of the solution corresponding to the minimum value of $\chi^2_{\rm ecl}$ along with the light-curve data for the night on which the eclipse occurs. This solution predicts a period of 58±12 d and an inclination of 89.1° ± 0.3°.

### 6.8 INT-7789-TR-2

TR-2 shows a single 0.02 mag eclipse of duration 2.5 h during the 2000–09 run (Fig. 12d). With $r' \approx 18.02$ mag and $r' - i' \approx 0.47$ mag, we find that the primary is a 1.20 $M_\odot$ F star at $d = 5.3$ kpc, behind the cluster. A central transit fit to the 2000–09 data yields a minimum companion radius of 0.174 $R_\odot$, from which we cannot rule out the transiting planet model.

Applying the same analysis as for EB-21 in Section 6.6 to the single eclipse yields a predicted period of 0.62 d for $b = 0$ that increases slowly with increasing values of $b$. For $b < 0.66$, $\chi^2_{\rm fold} \gg \chi^2_{\rm ecl}$, and for $b \geqslant 0.66$, $\chi^2_{\rm fold}$ oscillates between the states $\chi^2_{\rm fold} \gg \chi^2_{\rm ecl}$ and $\chi^2_{\rm fold} = \chi^2_{\rm ecl}$. Hence we can be sure that $b \geqslant 0.66$, which corresponds to $R_{\rm c}/R_* \geqslant 0.137$. In Fig. 12(c) we plot $\chi^2_{\rm ecl}$ versus $R_{\rm c}/R_*$ (dashed line) and $\chi^{2\prime}_{\rm fold}$ versus $R_{\rm c}/R_*$ (continuous line), where

$$\chi^{2\prime}_{\rm fold} = \begin{cases} \chi^2_{\rm fold} & \text{if } b < 0.66, \\ \chi^2_{\rm ecl} & \text{if } b \geqslant 0.66. \end{cases} \quad (19)$$

The minimum value of $\chi^2_{\rm ecl}$ obtained is $\chi^2_{\rm ecl} = 806.6$ corresponding to $R_{\rm c}/R_* = 0.137$, and this is marked on Fig. 12(c) as a horizontal shorter dashed line, along with the chi-squared values $\chi^2_{\rm ecl} = 806.6 + 1.0$, $\chi^2_{\rm ecl} = 806.6 + 4.0$ and $\chi^2_{\rm ecl} = 806.6 + 9.0$ corresponding to the $1\sigma$, $2\sigma$ and $3\sigma$ confidence levels.

One can see from Fig. 12(c) that $0.137 \leqslant R_{\rm c}/R_* \leqslant 0.144$ with a $1\sigma$ confidence. This is equivalent to stating that $R_{\rm c} = 0.185^{+0.009}_{-0.000}\,R_\odot$. Hence the conclusion at the $1\sigma$ level is that this is a possible transiting planet in orbit around a 1.20 $M_\odot$ F star that merits follow-up observations. Fig. 12(d) shows a plot of the solution corresponding to the minimum value of $\chi^2_{\rm ecl}$ along with the light-curve data for the night on which the eclipse occurs. This solution predicts a period of 1.8 ± 1.3 d and an inclination of 81.9° ± 1.6°.

### 6.9 INT-7789-TR-3

TR-3 exhibits two fully observed eclipses and one partially observed eclipse during the 2000–09 run. The eclipses have a depth of 0.07 mag and duration 1.7 h with a period of 1.24 d (Figs 12e, g and h). The star has $r' \approx 19.55$ mag and $r' - i' \approx 0.97$ mag, from which we derive a 0.68 $M_\odot$ primary star of spectral type K5V that lies slightly in front of the cluster ($d = 2.0$ kpc). A full transit fit to the 2000–09 light-curve data yields a best-fitting companion radius of 0.151 ± 0.007 $R_\odot$ consistent with the radius of a transiting planet (Fig. 12f). This solution is reported in Table 7 under model B, and the $\chi^2$ of the fit is 729.99.

However, there are two other models for TR-3 that should be considered to see if they produce a better $\chi^2$ value for the fit to the light-curve data. It is possible that the companion is a smaller and less luminous star than the primary star and produces a secondary eclipse that is not visible in the light curve folded at the ∼1.24 d period; and it is also possible that the companion is a star of similar size and luminosity to the primary star and that the system actually has an orbital period of ∼2.48 d. In order to test these models for TR-3, we have developed an eclipsing binary model based on the same assumptions as for the star and planet system presented in Section 6.1 except that we assume that the companion is now luminous and massive, and that our theoretical main-sequence relationships adopted in Section 4.3 apply to the companion.

The eclipsing binary model has five parameters to optimize: orbital period $P$, time of mid-eclipse $t_0$, orbital inclination $i$, companion to primary star radius ratio $R_{\rm c}/R_*$ and a constant magnitude $m_0$. We fitted this model to the light curve of TR-3 by calculating the $\chi^2$ for a grid in $i$ and $R_{\rm c}/R_*$. For each value of $R_{\rm c}/R_*$, we had to recalculate the distance $d$ to the system, the values of $M_*$ and $R_*$ for the primary star, and the mass of the companion $M_{\rm c}$. This was done by constructing a theoretical binary main sequence for the current value of $R_{\rm c}/R_*$ and then finding the distance $d$ such that this model passes through the position of TR-3 in the colour–magnitude domain. The initial value of $P$ was either 1.24 d or 2.48 d corresponding to the smaller or similar size stellar companion models respectively. Table 7 reports the results of these fits. Fig. 13 shows a chi-squared contour map, a folded and binned light curve with the best-fitting eclipsing binary model, an unbinned close-up of the folded light curve around the primary eclipse along with the best-fitting model, and another unbinned close-up around the secondary eclipse along with the best-fitting model. The left-hand column of diagrams in

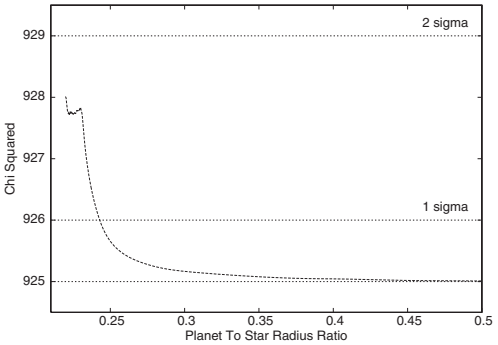


(a) **TR-1** - $\chi^2_{\rm ecl}$ (dashed line) versus $R_{\rm c}/R_*$ - 2000-09

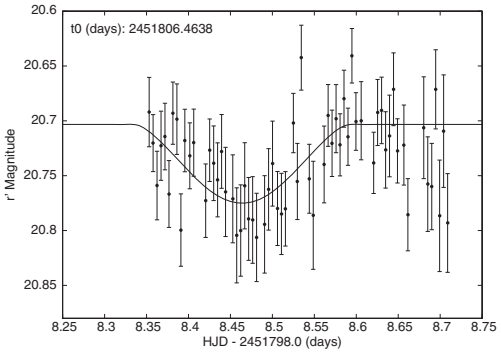


(b) **TR-1** - L & Single Eclipse Fit - 2000-09 Night 9

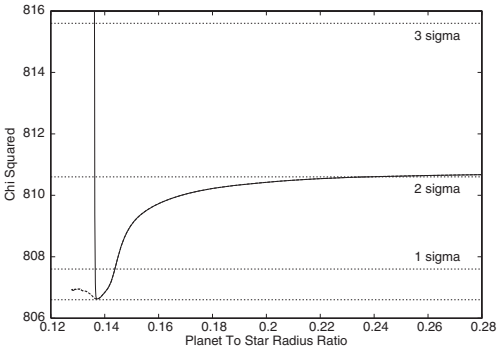


(c) **TR-2** - $\chi^2_{\rm ecl}$ (dashed line) versus $R_{\rm c}/R_*$ & $\chi^2_{\rm fold}$ (continuous line) versus $R_{\rm c}/R_*$ - 2000-09

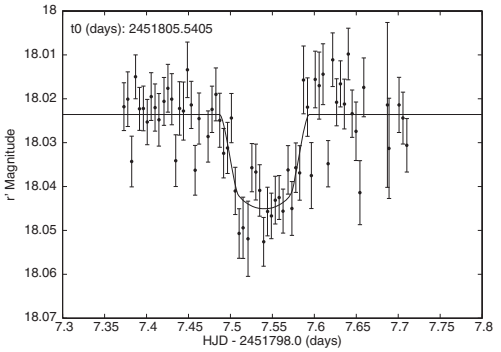


(d) **TR-2** - L & Single Eclipse Fit - 2000-09 Night 8

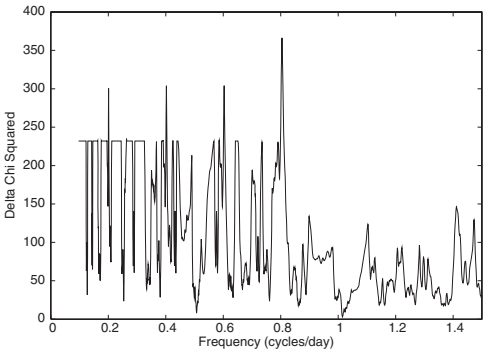


(e) **TR-3** - Eclipse Periodogram - 2000-09

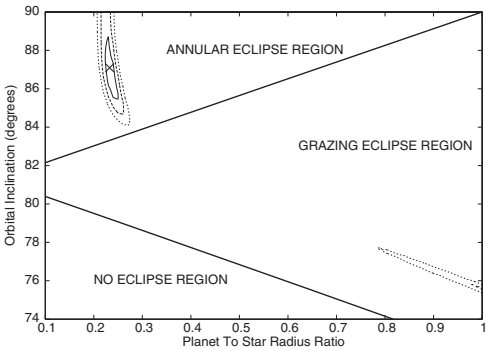


(f) **TR-3** - CM - 2000-09

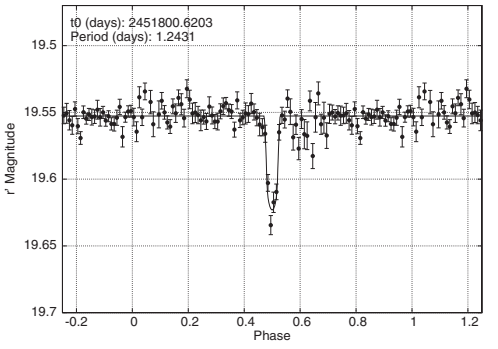


(g) **TR-3** - PL, BL & FTFIT - 2000-09

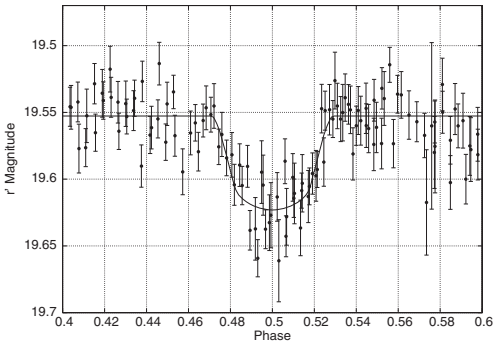


(h) **TR-3** - CPL & FTFIT - 2000-09

**Figure 12.** Planetary transit candidates TR-1, TR-2 and TR-3.

**Table 7.** Star, companion and light-curve properties for TR-3 as obtained from the various fits detailed in Section 6.9. Column 4 is calibrated $r'$ magnitude. $M_c$ and $R_c$ are the companion mass and radius, respectively. The ratio $f_c/f_*$ is the flux ratio of the companion to the primary star in the Sloan $r'$ waveband. The quantity $d$ is the distance to the system.

| Model | $t_0 - 245\,1000.0$ (d) | $P$ (d) | $m_0$ ($r'$ mag) | $m$ (mag) | $t$ (h) | $i$ (°) | $M_*$ ($M_\odot$) | $R_*$ ($R_\odot$) | $M_c$ ($M_\odot$) | $R_c$ ($R_\odot$) | $f_c/f_*$ (Sloan $r'$) | $d$ (pc) | $\chi^2$ |
|---|---|---|---|---|---|---|---|---|---|---|---|---|---|
| A | 800.6201(7) | 2.4867(116) | 19.553 | 0.086 | 1.93 | 83.48(6) | 0.701(5) | 0.670(5) | 0.661(30) | 0.629(29) | 0.669 | 2788(6) | 725.88 |
| B | 800.6203(7) | 1.2431(58) | 19.553 | 0.070 | 1.72 | 87.1(1.2) | 0.679(4) | 0.649(4) | 0.000 | 0.151(7) | 0.000 | 1995(5) | 729.99 |
| C | 800.6204(7) | 1.2430(58) | 19.553 | 0.070 | 1.68 | 88.8(1.5) | 0.682(4) | 0.651(4) | 0.126(6) | 0.149(6) | 0.0019 | 2021(5) | 731.73 |

Models: A = similar size stellar companion; B = planetary companion; C = small stellar companion.

Fig. 13 applies to the case of the smaller stellar companion and the right-hand column of diagrams in Fig. 13 applies to the case of the similar size stellar companion.

Table 7 shows that the best model for TR-3 is the eclipsing binary model with a similar size stellar companion, since this model attains the smallest $\chi^2$ of 725.88. All three models require exactly five parameters to be optimized, and hence we calculate a likelihood ratio of ∼7.8 for the eclipsing binary model with a similar size stellar companion compared to the transiting planet model, and we calculate a likelihood ratio of ∼18.6 for the eclipsing binary model with a similar size stellar companion compared to the eclipsing binary model with a smaller stellar companion. Finally, we calculate a likelihood ratio of ∼2.4 for the transiting planet model compared to the eclipsing binary model with a smaller stellar companion. Hence our conclusion is that this system is most likely to be a grazing eclipsing binary with period 2.49 d consisting of a K4V star primary and a K5V star secondary that lies at $d = 2.8$ kpc, slightly behind the cluster. However, further observations will be required to confirm this conclusion and categorically rule out the transiting planet model.

### 6.10 Finding charts

In order to help facilitate follow-up observations of the eclipsing binaries and transit candidates presented in the preceding sections, we supply finding charts in Fig. 14. Each stamp is a $27 \times 27$ arcsec$^2$ section of the relevant reference frame, where north is up and east is to the right. Each eclipsing binary/transit candidate lies at the centre of its stamp and is marked by a cross.

## 7 CONCLUSIONS

In the search for our transit candidates, we have developed an accurate, efficient and fast photometry pipeline employing the technique of difference image analysis. Raw data from the telescope are processed by the pipeline with minimal user input in order to produce light curves and colour–magnitude diagrams directly. This is especially important considering the high quantity of data that may arise from a transit survey.

Our analysis of the colour–magnitude diagrams by including the treatment of extinction for the open cluster NGC 7789 has allowed us to assign a model-dependent mass, radius and distance to each star. Such information is vital in the subsequent analysis of the transit candidates, since it allows a direct estimate of the companion radius. We detected 24 transit candidates that warranted a detailed analysis of their light curves, and we were able to determine periods for 14 of these candidates. Of the 10 candidates without periods, we could rule out the transiting planet model for seven of them by determining the minimum companion radius and for another one by predicting the orbital period. For INT-7789-TR-1, it was only at the $1\sigma$ level that we could rule out the transiting planet model based on the shape of the best eclipse. For INT-7789-TR-2 we found a companion radius of $0.185^{+0.009}_{-0.000}\,R_\odot$ ($1.81^{+0.09}_{-0.00}\,R_J$) based on the analysis of the only eclipse. Follow-up observations (see below) will be required for both of these candidates in order to confirm that INT-7789-TR-1 is an eclipsing binary and in order to determine the nature of INT-7789-TR-2.

For the 14 transit candidates with well-determined periods, we could rule out the transiting planet model for four of them from the detection of previously disguised secondary eclipses, and for three of them from the observation that the out-of-eclipse light-curve data exhibit ellipsoidal variations and heating effects. One of the candidates is possibly a new cataclysmic variable with a long period (10.8 h), which could be a cluster member, worthy of follow-up observations in its own right. All of the eight above-mentioned candidates plus another five may be ruled out as having planetary companions by considering that the companion radius obtained from the full transit fit is greater than $0.2\,R_\odot$. For INT-7789-TR-3, none of the above arguments may be used to rule out the transiting planet model. However, on application of an eclipsing binary model to the light curve we find that the model consisting of a pair of grazing K dwarf stars is ∼7.8 times more likely than the transiting planet model. This is by no means a definitive conclusion that INT-7789-TR-3 is an eclipsing binary, since there is a non-negligible probability that the transiting planet model is still valid. Follow-up observations will be required to confirm that INT-7789-TR-3 is the type of eclipsing binary that we predict in this paper.

Future photometric observations of the three transit candidates for which we could not rule out the transiting planet model with confidence should consist of time-series observations in two different filters. Eclipsing binary status may be confirmed by the observation of different eclipse depths in different filters, since a planetary transit is an achromatic event. INT-7789-TR-1 and INT-7789-TR-2 also require the observations of multiple eclipses in order to determine their period and whether they exhibit secondary eclipses or not. If these follow-up photometric observations still allow the possibility that the transiting planet model is valid, then radial velocity observations may be used to place an upper limit on the mass of the orbiting companion, hopefully low enough to rule out a stellar or brown dwarf companion. The fact that these candidates are so faint ($r' \approx 20.7$ mag for INT-7789-TR-1, $r' \approx 18.0$ mag for INT-7789-TR-2, and $r' \approx 19.6$ mag for INT-7789-TR-3) makes it very unlikely that radial velocity observations with 10-m class telescopes will achieve the accuracy required to determine the actual mass of the companion (Charbonneau 2003).

From a simple signal-to-noise ratio argument presented in Section 4.5, we expected to detect ∼2 transiting hot Jupiters. At most we have detected three transiting hot Jupiters, but our analysis of these candidates shows that this is very unlikely. Follow-up observations

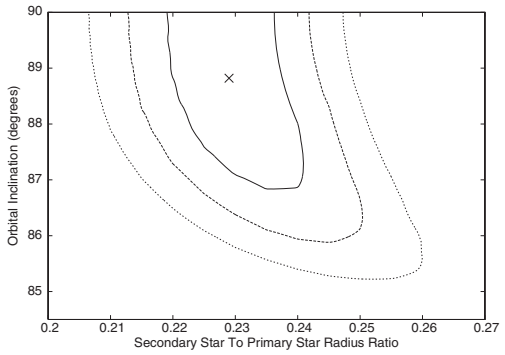


(a) **TR-3** - CM - 2000-09

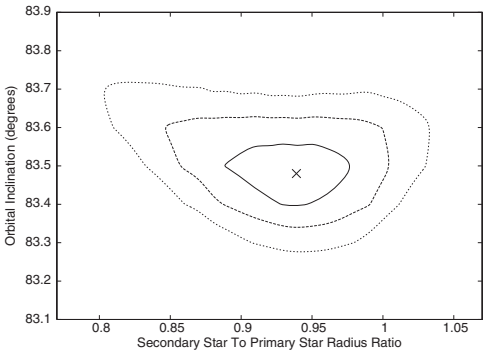


(b) **TR-3** - CM - 2000-09

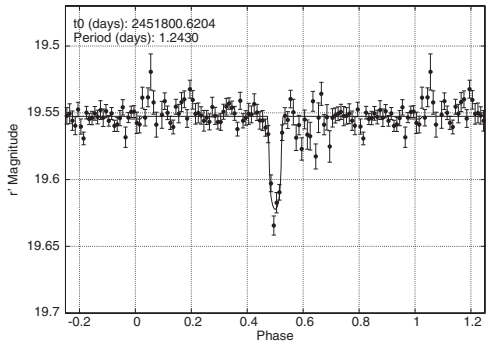


(c) **TR-3** - PL, BL & Eclipsing Binary Fit - 2000-09

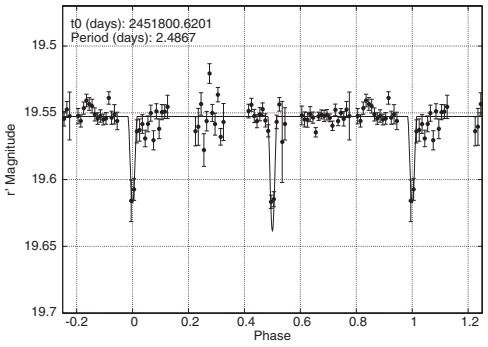


(d) **TR-3** - PL, BL & Eclipsing Binary Fit - 2000-09

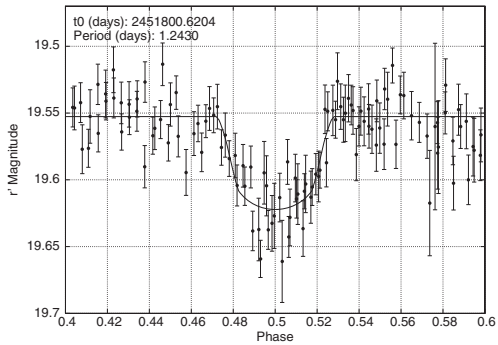


(e) **TR-3** - CPL & Eclipsing Binary Fit - 2000-09

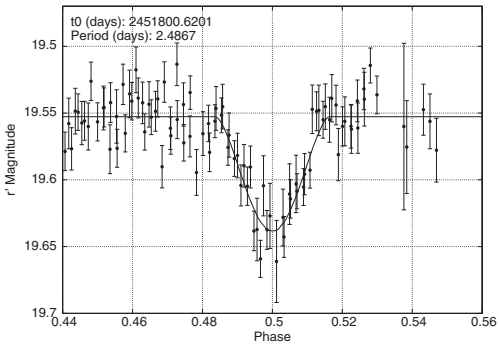


(f) **TR-3** - CPL & Eclipsing Binary Fit - 2000-09

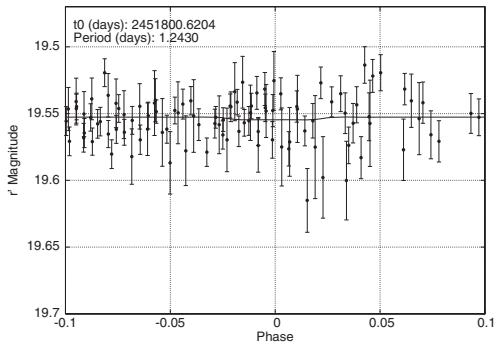


(g) **TR-3** - CPL & Eclipsing Binary Fit - 2000-09

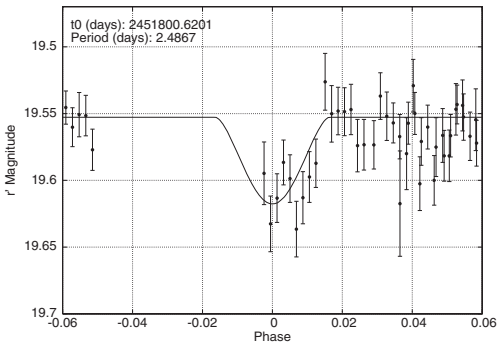


(h) **TR-3** - CPL & Eclipsing Binary Fit - 2000-09

**Figure 13.** Eclipsing binary fits for TR-3.

will most likely show that our candidates are eclipsing binaries, which means that our transit survey will have produced a null result. We are currently modelling in more detail the number of hot Jupiters that we expected to detect as a function of planetary radius, orbital period, star mass and detection threshold via Monte Carlo simulations. The results of these simulations are consistent with our simple estimate of the expected number of detections, and by combining this information with the results of further observations on

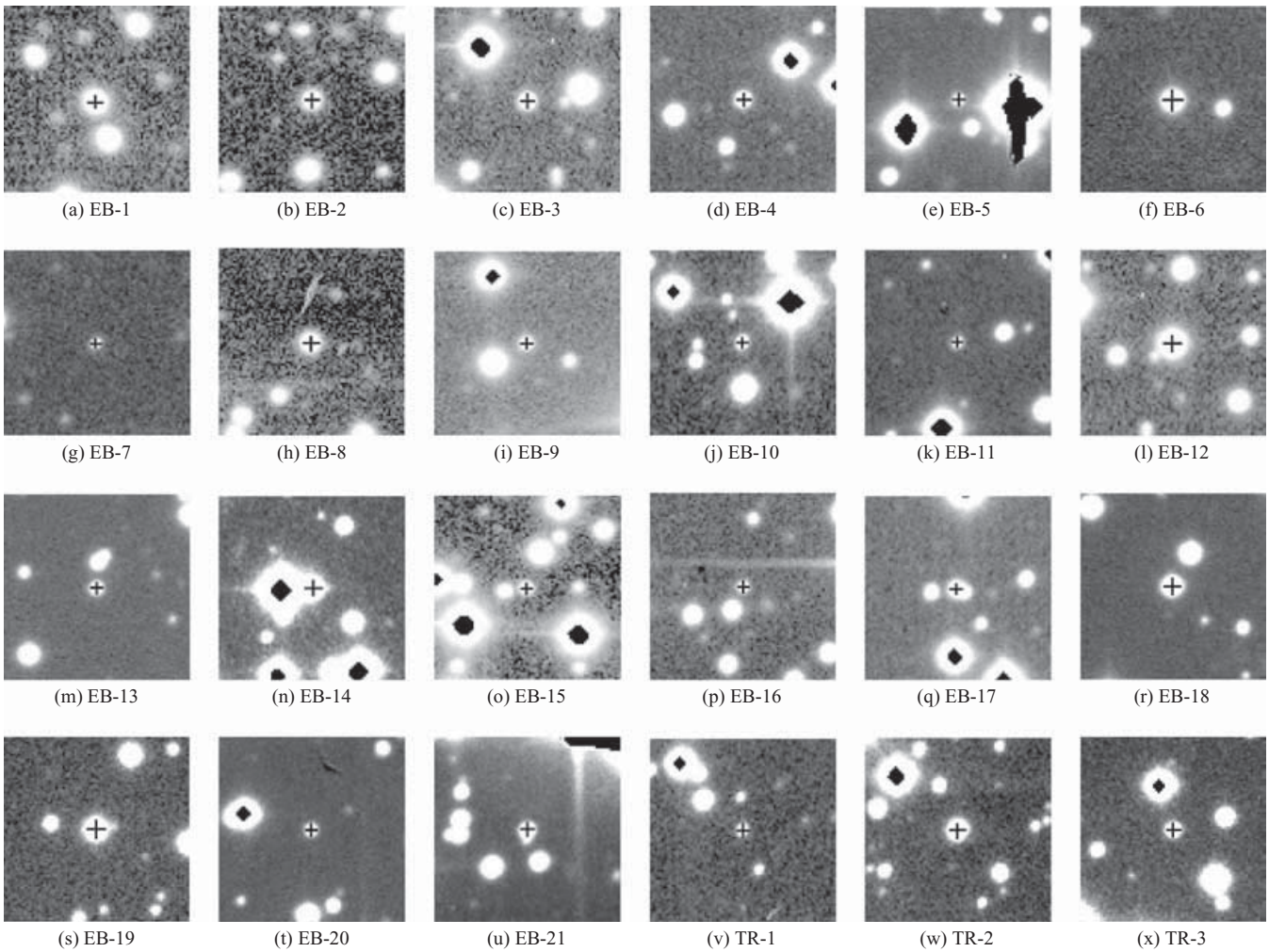


**Figure 14.** Finding charts taken from the reference frames; north is up and east is to the right. The stamps are of size 27 × 27 arcsec$^2$. Each eclipsing binary/transit candidate lies at the centre of its stamp and is marked by a cross.

the three remaining transit candidates, we will be able to estimate the hot Jupiter fraction of the cluster field, a very important result for the testing of star and planetary formation theories.

## ACKNOWLEDGMENTS

This research made use of the Simbad data base operated at CDS, Strasbourg, France, and the WEBDA data base operated at the University of Lausanne, Switzerland. This paper was based on observations made with the Isaac Newton Telescope operated by the Isaac Newton Group on the island of La Palma in the Spanish Observatorio del Roque de los Muchachos. DMB was funded by a PPARC research studentship during the course of this work, and would like to thank both St. Andrews University, Scotland, and the Instituto de Astrofisica de Canarias, Spain, for their hospitality during this time. A special thanks goes to Rocio Muñiz Santacoloma, who provided the inspiration and support necessary in order to complete this work.

## REFERENCES

Alard C., 2000, A&AS, 144, 363
Alard C., Lupton R. H., 1998, ApJ, 503, 325
Alonso R. et al., 2004, ApJ, 613, L153
Arellano Ferro A., Arévalo M. J., Lázaro C., Rey M., Bramich D. M., Giridhar S., 2004, Rev. Mex. Astron. Astrofis., 40, 209
Baraffe I., Chabrier G., Allard F., Hauschildt P. H., 1998, A&A, 337, 403
Bond I. A. et al., 2001, MNRAS, 327, 868
Bouchy F., Pont F., Santos N. C., Melo C., Mayor M., Queloz D., Udry S., 2004, A&A, 421, L13
Brown T. M., Charbonneau D., Gilliland R. L., Noyes R. W., Burrows A., 2001, ApJ, 552, 699
Burke C. J., Gaudi B. S., DePoy D. L., Pogge R. W., Pinsonneault M. H., 2004, AJ, 127, 2382
Butler R. P., Marcy G. W., Vogt S. S., Fischer D. A., 2000, in Penny A., Artymowicz P., Lagrange A.-M., Russell S., eds, Proc. IAU Symp. 202, Planetary Systems in the Universe: Observation, Formation and Evolution. Astron. Soc. Pac., San Francisco
Charbonneau D., 2003, preprint (astro-ph/0302216)
Charbonneau D., Brown T. M., Latham D. W., Mayor M., 2000, ApJ, 529, L45
Charbonneau D., Brown T. M., Dunham E. W., Latham D. W., Looper D. L., Mandushev G., 2004, in Holt S. S., Deming D., eds, AIP Conf. Proc. Vol. 713, The Search for Other Worlds. Am. Inst. Phys, p. 151
Drake A. J., 2003, ApJ, 589, 1020
Drake A. J., Cook K. H., 2004, ApJ, 604, 379
Draper P. W., 2000, in Manset N., Veillet C., Crabtree D., eds. ASP Conf. Ser. Vol. 216, Astronomical Data Analysis Software and Systems IX. Astron. Soc. Pac., San Francisco, p. 615
Gim M., Vandenberg Don A., Stetson P. B., Hesser J. E., Zurek D. R., 1998, PASP, 110, 1318
Hood B. et al. 2005, MNRAS, submitted

Konacki M., Torres G., Jha S., Sasselov D. D., 2003, Nat, 421, 507
Konacki M. et al., 2004, ApJ, 609, L37
Konacki M., Torres G., Sasselov D. D., Jha S., 2005, ApJ, in press (astro-ph/0412400)
Lang K. R., 1992, Astrophysical Data: Planets and Stars. Springer, Berlin
Lee B. L., von Braun K., Malten-Ornelas G., Yee H. K. C., Seager S., Gladders M. D., 2004, Holt S. S., Dening D., eds, AIP Conf. Proc. 713, The Search for Other Worlds. Am. Inst. Phys., New York, p. 177
Mallén-Ornelas G., Seager S., Yee H. K. C., Minniti D., Gladders M. D., Mallén-Fullerton G. M., Brown T. M., 2003, ApJ, 582, 1123
Mazeh T. et al., 2000, ApJ, 532, L55
Mochejska B. J., Stanek K. Z., Sasselov D. D., Szentgyorgyi A. H., 2002, AJ, 123, 3460
Mochejska B. J., Stanek K. Z., Sasselov D. D., Szentgyorgyi A. H., Westover M., Winn J. N., 2004, AJ, 128, 312
Monet D. G. et al., 2003, AJ, 125, 984
Pont F., Bouchy F., Queloz D., Santos N. C., Melo C., Mayor M., Udry S., 2004, A&A, 426, L15
Robin A. C., Crézé M., Mohan V., 1992, ApJ, 400, L25
Robin A. C., Reylé C., Derriére S., Picaud S., 2003, A&A, 409, 523
Schneider J., 1996, http://www.obspm.fr/encycl/cat1.html
Seaton M. J., 1979, MNRAS, 187, 73
Sirko E., Paczyński B., 2003, ApJ, 592, 1217
Stetson P. B., 1987, PASP, 99, 191
Street R. A. et al., 2003, MNRAS, 340, 1287
Udalski A. et al., 2002a, Acta Astron., 52, 1
Udalski A., Zebrun K., Szymanski M., Kubiak M., Soszynski I., Szewczyk O., Wyrzykowski L., Pietrzynski G., 2002b, Acta Astron., 52, 115
Udalski A., Pietrzynski G., Szymanski M., Kubiak M., Zebrun K., Soszynski I., Szewczyk O., Wyrzykowski L., 2003, Acta Astron., 53, 133
von Braun K., Lee B. L., Mallen-Ornelas G., Yee H. K. C., Seager S., Gladders M. D., 2004a, http://www.ciw.edu/kaspar/OC_transits/OC_transits.html
von Braun K., Lee B. L., Malten-Ornelas G., Yee H. K. C., Seager S., Gladders M. D., 2004b, AIP Conf. Proc. 713, The Search for Other Worlds, Am. Inst. Phys., New York, p. 181
Wallace P. T., 1998, Starlink User Note 5.17, Rutherford Appleton Laboratory
Walton N. A., Lennon D. J., Greimel R., Irwin M. J., Lewis J. R., Rixon G. T., 2001, ING Newslett., 4, 7

This paper has been typeset from a TEX/LATEX file prepared by the author.